

Recent advances in multiferroics and magnetoelectrics

Zhen Liu(刘振), Jing-Bo Zhou(周靖博), Pin-Yi Zeng(曾品一), Hao-Wen Wang(王好文), and Cheng-Liang Lu(陆成亮)

Citation: Chin. Phys. B, 2026, 35 (**7**): 077504. DOI: 10.1088/1674-1056/ae395c
http://cpb.iphy.ac.cn; http://iopscience.iop.org/cpb

What follows is a list of articles you may be interested in

The rise of van der Waals multiferroic heterostructures: Interfacial physics and devices

Yihao Zhao(赵一豪), Hongxu Duan(段虹旭), Tai Min(闵泰), and Tao Li(李桃)
Chin. Phys. B, 2026, 35 (**6**): 067501. DOI: 10.1088/1674-1056/ae3e73

Magnetoelectric topology: The rope weaving in parameter space

Ying Zhou(周颖), Ziwen Wang(王子文), Fan Wang(王凡), Haoshen Ye(叶浩燊), and Shuai Dong(董帅)
Chin. Phys. B, 2026, 35 (**2**): 027501. DOI: 10.1088/1674-1056/ae2c6b

Structural evolution-enabled $BiFeO_3$ modulated by strontium doping with enhanced dielectric, optical and superparamagnetic properties by a modified sol-gel method

Sharon V S, Veena Gopalan E, and Malini K A
Chin. Phys. B, 2023, 32 (**3**): 037504. DOI: 10.1088/1674-1056/ac785b

Computational studies on magnetism and ferroelectricity

Ke Xu(徐可), Junsheng Feng(冯俊生), and Hongjun Xiang(向红军)
Chin. Phys. B, 2022, 31 (**9**): 097505. DOI: 10.1088/1674-1056/ac7b1b

Intrinsic two-dimensional multiferroicity in $CrNCl_2$ monolayer

Wei Shen(沈威), Yuanhui Pan(潘远辉), Shengnan Shen(申胜男), Hui Li(李辉), Siyuan Nie(聂思媛), and Jie Mei(梅杰)
Chin. Phys. B, 2021, 30 (**11**): 117503. DOI: 10.1088/1674-1056/ac0787

TOPICAL REVIEW — Multiferroicity and multicaloric effects

Recent advances in multiferroics and magnetoelectrics

Zhen Liu(刘振), Jing-Bo Zhou(周靖博), Pin-Yi Zeng(曾品一),
Hao-Wen Wang(王好文), and Cheng-Liang Lu(陆成亮)†

School of Physics and Wuhan National High Magnetic Field Center, Wuhan 430074, *China*

(Received 7 November 2025; revised manuscript received 4 January 2026; accepted manuscript online 16 January 2026)

Multiferroics, where multiple ferroic orders coexist and couple, have been one of the most active fields in condensed matter physics over the past two decades. In particular, the cross-control between magnetic and electric variables, i.e., the magnetoelectric coupling effect, provides a unique advantage for developing low-consumption electronic devices. In recent years, the field has seen a fundamental expansion of its scope to include topological magnetoelectricity and two-dimensional (2D) multiferroics. This review mainly focuses on the progress made in the last decade, covering new material exploration and emerging physical phenomena. It begins with an overview of linear magnetoelectricity, continues with detailed discussions of emerging topological magnetoelectricity and 2D multiferroics, and ends with an outlook on future developments for multiferroicity and magnetoelectric coupling.

Keywords: multiferroics, magnetoelectric coupling, linear magnetoelectric effect, topological magnetoelectricity, two-dimensional multiferroics

PACS: 75.85.+t, 75.25.–j, 75.25.Dk, 71.70.Ej

DOI: 10.1088/1674-1056/ae395c **CSTR:** 32038.14.CPB.ae395c

1. Introduction

Multiferroic materials often specifically refer to compounds exhibiting both magnetism and ferroelectricity, which allow for electric field (E) control of magnetization (M) and magnetic field (H) manipulation of ferroelectric (FE) polarization (P). Such materials have significant potential for applications in low-consumption information storage and ultrasensitive sensors.[1–4] The magnetoelectric (ME) effect can be traced back to Pierre Curie's theoretical predictions in 1894, postulating the possibility of such a coupling based on symmetry arguments. The antiferromagnet Cr_2O_3 was the first compound in which the ME effect was experimentally verified in the 1960s. Following this discovery, the field of ME research was launched.

The ME effect can be understood within the framework of Landau theory, approached by an expansion of the free energy for a magnetoelectric system. From a thermodynamic perspective, the free energy (F) for single-phase ME materials can be expanded in a Taylor series in powers of E and H, yielding the expression:

$$-F(E,H) = \frac{1}{2}\varepsilon_{ij}E_iE_j + \frac{1}{2}\mu_{ij}H_iH_j + \alpha_{ij}E_iH_j + \frac{1}{2}\beta_{ijk}E_iH_jH_k + \frac{1}{2}\gamma_{ijk}H_iE_jE_k + \cdots, \quad (1)$$

where tensors ε_{ij} and μ_{ij} are the electric and magnetic susceptibilities, and tensor α_{ij} is the linear ME coefficient.[5] As the most intensively studied ME phenomenon since the 1960s, linear ME is characterized by a linear dependence of M on E ($\mu_0 M_i = \alpha_{ji}E_j$), or conversely, of the polarization P on H ($P_i = \alpha_{ij}H_j$). The intertwining of broken time-reversal symmetry and space-inversion symmetry in linear ME has led to a series of emergent phenomena, such as the ME monopole, ferrotoroidicity, and non-reciprocal transport of quasiparticles.[4,6–9] A long-term issue for linear ME activities is the weak ME coupling and thereby small coefficient α.[10–12] Utilization of spin–lattice coupling presents a promising framework to address this challenge, which has been experimentally verified in several materials in recent years.[11–14]

It was not until the discovery of type-II multiferroics in 2003 that research on the ME effect witnessed a major breakthrough. Wang *et al.* synthesized high-quality $BiFeO_3$ epitaxial thin films, which exhibit excellent ferroelectricity and notable ME coupling at room temperature (T).[15] Meanwhile, Kimura *et al.* discovered magnetically-driven ferroelectricity in $TbMnO_3$, in which the P-direction can be flipped by an external H.[15,16] In the following year, Cheong's group reported similar magnetically-driven ferroelectricity and a striking ME effect in $TbMn_2O_5$.[17] In these multiferroics, the ME effect can be unprecedentedly strong due to the first-order phase transition, resulting in a high-order ME effect. These discoveries have spurred the advancement in the research of multiferroics and magnetoelectrics, which can be found in many previous high-quality review articles.

Over the past decade, this promising discipline has en-

†Corresponding author. E-mail: cllu@hust.edu.cn

© 2026 Chinese Physical Society and IOP Publishing Ltd. All rights, including for text and data mining, AI training, and similar technologies, are reserved.

tered a new era, marked by two key developments. First, the integration of topology and multiferroics. Fascinating textures of magnetic and/or electric dipoles in real space have been widely identified in multiferroic materials, including magnetic skyrmions, ferroelectric vortex domains, and merons with integer winding numbers.[6,18–23] Recently, a topologically nontrivial ME switching effect was unveiled in several multiferroics such as $GdMn_2O_5$,[24,25] $TbMn_3Cr_4O_{12}$,[26] and a GdI_2 monolayer.[27] The topological ME describes topological functions in the ME parameter phase space, fundamentally different from the topology in momentum and real spaces. Second, two-dimensional (2D) multiferroics hold great promise for miniaturized and high-efficiency integrated devices.[28,29] Their flexible structures and tunable symmetries allow the realization of magnetoelectric states with strongly enhanced coupling among multiple degrees of freedom, including spin, valley, lattice, and charge.[30] In these systems, twisting the interlayer angle can create moiré superlattices that host novel magnetoelectric phases.[31,32] Interlayer sliding enables atomic-scale control of polarization and magnetic exchange.[33,34] Meanwhile, the valley degree of freedom interacts with spin and polarization through spin–orbit coupling, leading to valley-selective magnetoelectric effects and spin–valley coupling.[35] Together, these features reshape the electronic structure and the interplay between spin, charge, and lattice in 2D materials.

This review will focus on the progress achieved in the past decade. We begin with a brief overview of advancements in linear ME materials. Subsequent sections discuss cutting-edge research on topological magnetoelectric effects and emerging 2D multiferroics, before concluding with an outlook on the future of multiferroicity and ME coupling.

2. Linear magnetoelectricity

The linear ME effect is defined as the induction of an electric P by H, and vice-versa, which was first discovered in Cr_2O_3. The recent progress is twofold. First, a series of novel phenomena have been found even in well-established linear ME systems like Cr_2O_3. Second, a significant number of linear ME materials have been synthesized. Listed in Table 1 are the basic properties of some linear ME materials.

Table 1. Basic properties of some linear ME materials.

Material	Magnetic phase transition	Space group	Magnetic space group	Magnetic point group	Linear ME coefficient α
Cr_2O_3[8]	$T_N \sim 307$ K	$R\bar{3}c$	$R\bar{3}'c'$	$-3'm'$	~ 4.2 ps/m
$Mn_4Nb_2O_9$[36]	$T_N \sim 110$ K	$P\bar{3}c1$	$P\bar{3}'c'1$	$-3'm'$	~ 2.1 ps/m
$Co_4Nb_2O_9$[37]	$T_N \sim 27$ K	$P\bar{3}c1$	$C2/c'$	$2/m'$	~ 40 ps/m
$Fe_4Nb_2O_9$[38]	$T_{N1} \sim 90$ K and $T_{N2} \sim 77$ K	$P\bar{3}c1$	$C2/c'$	$-1'$	~ 25 ps/m
$Fe_2Mo_3O_8$[39]	$T_N \sim 60$ K	$P6_3mc$	$P6_3'm'c$	$6'mm'$	~ 480 ps/m
$Mn_2Mo_3O_8$[40]	$T_C \sim 41.5$ K	$P6_3mc$	$P6_3'm'c$	$6m'm'$	~ 5 ps/m
$Co_2Mo_3O_8$[41]	$T_N \sim 39$ K	$P6_3mc$	$P6_3'm'c$	$6'mm'$	~ 28 ps/m
$Ni_2Mo_3O_8$[42]	$T_N \sim 5.5$ K	$P6_3mc$	P_cna2_1	$mm2$	~ 70 ps/m
Ni_3TeO_6[43]	$T_N \sim 54$ K	$R3$	$R\text{-}3'm'$	$-3'm'$	~ 36 ps/m
Ni_2CoTeO_6[43]	$T_N \sim 54$ K	$R3$	$R\text{-}3'm'$	$-3'm'$	~ 3.4 ps/m
$NiCo_2TeO_6$[43]	$T_N \sim 49$ K	$R3$	$R\text{-}3'm'$	$-3'm'$	~ 323 ps/m
$Mn_3Ta_2O_8$[12]	$T_N \sim 24$ K	$I4_1/a$	$P2_1/a$	$2'/m$	~ 5.6 ps/m
$DyCrO_4$[44]	$T_N \sim 24$ K	$I4_1/a$	$I4_1/a'$	$2'/m$	~ 50 ps/m
Cu_3TeO_6[45]	$T_N \sim 61$ K	$Ia\bar{3}$	$R\text{-}3'$	$-3'$	~ 3.1 ps/m
$LiCoPO_4$[46]	$T_N \sim 21.9$ K	$Pnma$	$P21'/c$	$2'/m$	~ 30.6 ps/m
$LiNiPO_4$[47]	$T_N \sim 20.8$ K	$Pnma$	$Pnm'a$	$m'mm$	~ 1.5 ps/m
$NdCrTiO_5$[48]	$T_N \sim 20$ K	$Pbam$	$Pbam'$	$m'mm$	~ 3.5 ps/m
$CoSe_2O_5$[49]	$T_N \sim 8.5$ K	$Pbcn$	$Pb'cn$	mmm'	~ 21.3 ps/m
Sm_2BaCuO_5[11]	$T_{N1} \sim 23$ K and $T_{N2} \sim 5$ K	$Pnma$	$Pn'ma$	mmm'	~ 4.4 ps/m
$Ni_5(TeO_3)_4Cl_2$[50]	$T_N \sim 29.2$ K	$C2/c$	$C2'/c$	$C2'/c$	~ 4.2 ps/m
$Co_5(TeO_3)_4Cl_2$[51]	$T_N \sim 18$ K	$C2/c$	$C2'/c$	$2'/m$	~ 45 ps/m
$MnPSe_3$[52]	$T_N \sim 70$ K	$R\bar{3}$	$P\bar{1}'$	$-1'$	~ 13.5 ps/m
Fe_2TeO_6[53]	$T_N \sim 208$ K	$P4_2/mnm$	$P4_2/m'nm'$	$4/m'm'm'$	~ 1.2 ps/m
$CoTe_6O_{13}$[54]	$T_N \sim 19.5$ K	$R\bar{3}$	$R\bar{3}\prime$	$-3'$	~ 41.2 ps/m

2.1. Chromium oxide

The discovery of the ME effect dates back to 1960 in chromium oxide (Cr_2O_3) with a high Néel temperature $T_N \sim 307$ K, which continues to be regarded as the prototypical linear ME material.[55–57] Recently, Iyama *et al.* revisited the ME effect in Cr_2O_3 single crystals and observed square-like $P(E)$ (and $M(H)$) hysteresis loops under finite H (and E).[8] These features imply that Cr_2O_3 behaves as a typical ferro-

electric (ferromagnet) under finite magnetic (electric) fields, even at room T. This hysteretic control enables switching and retaining the ME state, an ability that is essential for storage applications.

Cr_2O_3 has been used to develop purely antiferromagnetic (AFM) magnetoelectric random access memory (MERAM). This technology, free from ferromagnetic hysteresis loss, offers excellent energy efficiency, making it ideal for low-power data processing and storage devices.[58] The devices employ a polarizable paramagnet to detect the order parameter of the ME antiferromagnet, thereby circumventing issues arising from the presence of ferromagnetic components. Its writing threshold is significantly lower than that of traditional ferromagnetic magnetic random access memory (MRAM), with a reduction of about an order of magnitude, and it shows strong resistance to magnetic interference [Fig. 1(a)]. Using Cr_2O_3 as the AF element, a complete working AF-MERAM is demonstrated. The cell consists of an active layer of insulating ME antiferromagnet, a bottom-gate electrode for writing, and a top electrode for read-out via anomalous Hall measurement [Fig. 1(b)]. At room T, reliable isothermal switching and all-electrical read-out are achieved through gate voltage pulses, demonstrating the practical potential of linear ME for spintronic applications.

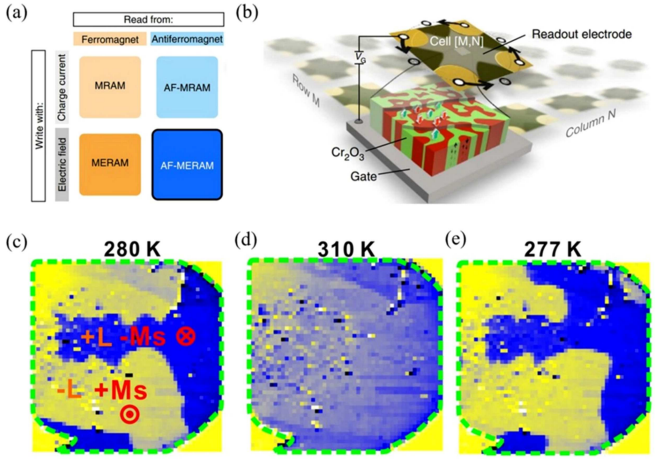


Fig. 1. (a) Magnetic random access memory elements are classified by their writing and readout interfaces. (b) Schematic of an AF-MERAM storage cell using Cr_2O_3.[58] (c)–(e) Magnetic domain images of Cr_2O_3 at different temperatures.[59]

Topological surface magnetism is another fascinating property of linear ME, which was recently observed in Cr_2O_3.[59] Scanning the sample surface reveals a clear magnetic circular dichroism (MCD) signal below T_N, indicating surface magnetization linked to AFM order. MCD images at 280 K reveal two AFM domains with opposite polarities and distinct surface magnetizations (+ and −) [Fig. 1(c)], indicating the presence of surface magnetization coupled with an AFM spin order. The domain pattern remains observable until 310 K, while the contrast gradually diminishes above 310 K [Fig. 1(d)], suggesting that surface magnetization vanishes above T_N. Upon cooling the sample back to 277 K, magnetic domains reemerge [Fig. 1(e)], further confirming the existence of surface magnetization. Notably, these surface magnetizations are highly sensitive to external magnetic fields. Applying opposing fields along the c-axis allows for continuous switching of the MCD signal's sign. Thus, unconventional Néel vector switching can be achieved solely through an applied magnetic field.

A spin superfluid ground state was observed at low T in Cr_2O_3 using non-local spin transport methods, which holds significance for fundamental research on the Bose–Einstein condensation of spin-1 bosons.[60] The mechanical strain gradient in Cr_2O_3 provides a basis for the magnetic and thermodynamic studies of AFM solitons and spin waves in magnetic materials.[61] Additionally, coherent nonlinear interactions between light and Cr_2O_3 can generate pure electronic macroscopic effects within the crystal, facilitating quantitative manipulation of magnetism via the electronic ME effect.[62] The enduring research on Cr_2O_3 continues to offer essential insights into linear ME coupling and its technological potential.

2.2. Honeycomb magnets of $A_4Nb_2O_9$ (A = Mn, Co, Fe)

The family of $A_4Nb_2O_9$ (A = Co, Mn, and Fe) with a honeycomb lattice is a new group of linear ME materials. The unique topological lattice introduces new dimensions to the control of ME coupling, establishing a complementary research avenue for structure–property modulation in comparison to the Cr_2O_3 system discussed above, and serving as a crucial platform for investigating topologically related linear ME effects. The $A_4Nb_2O_9$ compounds crystallize in a centrosymmetric triclinic space group $P\bar{3}c1$. A^{2+} ions occupy two inequivalent sites as $A(1)$ and $A(2)$, located at the centers of distorted octahedra formed by oxygen atoms. The $A(1)O_6$ octahedra are corner-connected, while the $A(2)O_6$ cages share edges, resulting in two distinct buckled honeycomb layers [Fig. 2(a)].[13]

$Mn_4Nb_2O_9$ undergoes an AFM transition at $T_N \sim 110$ K, which is nearly the highest Néel temperature among all $A_4Nb_2O_9$ compounds. Below T_N, the Mn^{2+} spins align along the c-axis, forming two opposite spin chains along lines of spin-up and spin-down, which are stabilized by the antiparallel inter-chain coupling [Fig. 2(b)]. The measured ME coupling tensor aligns well with the magnetic symmetry -3′m′, which is consistent with the linear ME scenario.[36] Nevertheless, a rather small linear ME coefficient of $\alpha \sim 2.1$ ps/m was reported in $Mn_4Nb_2O_9$.

$Co_4Nb_2O_9$ enters an AFM state below $T_N \sim 27$ K, which has been more extensively studied as compared with other members of $A_4Nb_2O_9$.[14] Single-crystal neutron diffraction experiments revealed that Co^{2+} magnetic moments primarily

lie in the basal plane, with neighboring moments in a honeycomb layer oriented oppositely and stacked along the trigonal axis [Fig. 2(c)], conforming to a magnetic structure of $C2/c'$.[13] Chang *et al.* reported an ultrarobust linear ME memory and training effect in $Co_4Nb_2O_9$.[37] The memory states exhibited distinct linear ME coefficients α across a wide H range. The $P(H)$ curve controlled by E is symmetric about the origin, and the two sets of ME coefficients α show opposite signs, indicating the dual controllability of H and E [Fig. 2(d)]. This phenomenon is attributed to AFM domain evolution, offering promising prospects for high-density and ultrafast switching in AFM spintronics. Mn-substitution at the Co-site in $Co_4Nb_2O_9$ can significantly enhance T_N, while gradually reducing the ME coefficient, a possible trade-off between the Néel point and ME coupling.[63]

In $Fe_4Nb_2O_9$, there are two phase transitions identified at $T_{N1} \sim 90$ K for an AFM transition and $T_{N2} \sim 77$ K for a structural phase transition.[38] Fe magnetic moments are primarily aligned in the *ab*-plane, akin to $Co_4Nb_2O_9$. A linear ME tensor α_{ij} with all nine nonzero components was experimentally measured, indicating a reduced magnetic point group of -1′ in this material.[64] The ME coupling effect is well explained by the p–d hybridization mechanism. The physical essence of this mechanism resides in the modulation of covalency between the d-orbitals of transition metals and the p-orbitals of ligands by the relativistic spin–orbit interaction, which depends on the orientation of the local spin magnetic moment. This process gives rise to local electric dipoles oriented along the bond direction.[1,65]

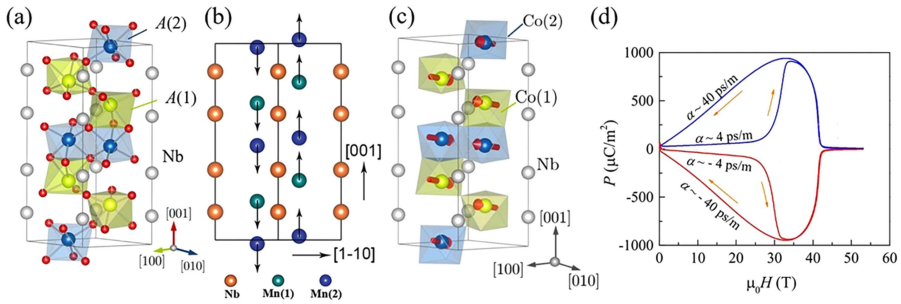


Fig. 2. (a) The crystal structure of $A_4Nb_2O_9$.[13] (b) The magnetic structures of $Mn_4Nb_2O_9$[36] and (c) $Co_4Nb_2O_9$.[13] (d) The dependence of P and the ME coefficient α on the magnetic field in $Co_4Nb_2O_9$.[37]

2.3. Polar magnets of $A_2Mo_3O_8$ (A = Fe, Mn, Co, Ni)

The polar magnet $A_2Mo_3O_8$ family (A = Fe, Mn, Co, and Ni) has attracted considerable attention recently. The intrinsic correlation between its ME response and the origin of structural polarity enhances the fundamental understanding of the coupling mechanism between multiferroicity and the linear ME effect, thereby further broadening the functional scope of linear ME materials. These materials belong to the noncentrosymmetric space group $P6_3mc$, where A^{2+} ions occupy both octahedral (OCT) and tetrahedral (TET) sites [Fig. 3(a)]. The crystal structure consists of alternating A_2 layers and Mo_3 layers along the c axis. The magnetism of this system arises from two types of unpaired 3d electrons in A^{2+} ions. This leads to diverse magnetic properties and complex magnetic orders, resulting in rich ME phenomena [Figs. 3(b) and 3(c)].

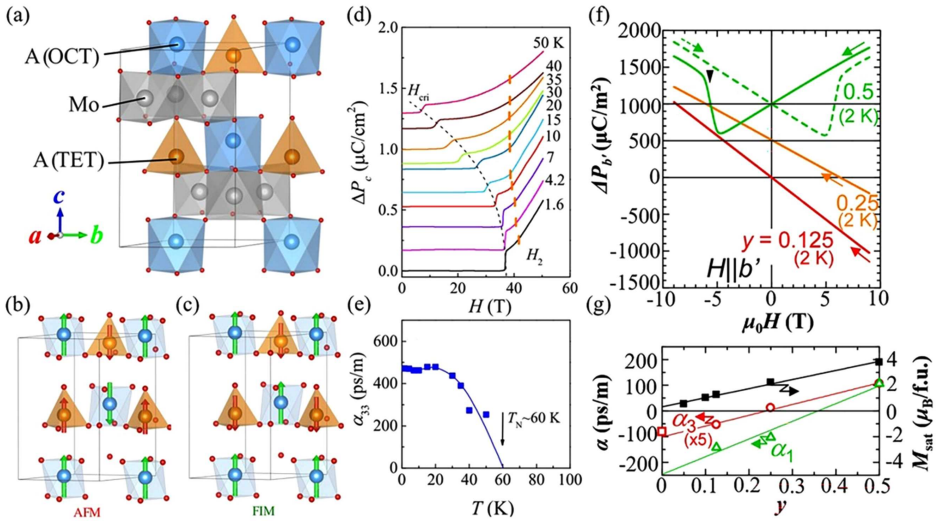


Fig. 3. (a) Crystal structure of $A_2Mo_3O_8$ family. (b) Schematic of AFM and (c) FIM orders, respectively.[41] (d) P of $Fe_2Mo_3O_8$ as a function of H measured at different temperatures. (e) T dependence of linear magnetoelectricity α_{33}.[39] (f) H dependence of ΔP in $(Fe_{1-y}Zn_y)_2Mo_3O_8$ ($y = 0.125, 0.25, 0.5$). (g) y dependence of ME coefficients α_1 ($\Delta P_c = \alpha_1 H_c$) and α_3 ($\Delta P_{b'} = \alpha_3 H_{b'}$).[67]

$Fe_2Mo_3O_8$ has an AFM phase below $T_N \sim 60$ K.[66] Chang *et al.* reported a colossal linear ME effect.[39] In the $\Delta P_c(H)$ curves measured at different temperatures, H_{cri} shifts to lower fields with increasing T, while H_2 shows minimal change, indicating distinct physical behaviors. At high magnetic fields, the curves exhibit clear linear behavior [Fig. 3(d)]. This effect persists in a wide magnetic field range of up to 20 T, with the diagonal component α_{33} reaching up to ~ 480 ps/m, which exceeds the values of most conventional linear ME materials by several orders of magnitude [Fig. 3(e)]. A theoretical model reproduced these observations, emphasizing contributions from the exchange striction mechanism and accounting for the sign difference of magnetocrystalline anisotropy. Tuning the magnetic ground state via chemical doping typically induces significant variations in the ME coupling effect. Kurumaji *et al.* showed that nonmagnetic Zn^{2+} doping suppresses the AFM order,[67] and stabilizes a ferrimagnetic (FRM) state, which is accompanied by sign reversal of the ME coefficient [Figs. 3(f) and 3(g)]. At a low Zn-doping level, strong competition between the AFM and FRM magnetic phases is induced, giving rise to multiple metamagnetic transitions in the $M(H)$ measurements.[68] It was found that slight Mg doping in $Fe_2Mo_3O_8$ can markedly enhance the ME effect for both the AFM ground state and the H-stabilized FRM phase.[69] The introduction of Ni into the $Fe_2Mo_3O_8$ structure has also yielded interesting results: a high-T glassy state was revealed, which offers a unique perspective for understanding other high-T phenomena in this system.[70]

$Co_2Mo_3O_8$ has an AFM ground state similar to $Fe_2Mo_3O_8$.[41] An AFM transition occurred at $T_N \sim 39$ K, accompanied by the appearance of P, indicating its magnetic origin. Unlike $Fe_2Mo_3O_8$, only a high-order ME effect was found in $Co_2Mo_3O_8$. High-field studies on $Co_2Mo_3O_8$ revealed two spin-flop transitions at $H_{c1} \sim 27$ T and $H_{c2} \sim 31$ T, accompanied by a large variation in P.[71]

$Mn_2Mo_3O_8$ has a FRM ground state below $T_C \sim 41.5$ K and exhibits orthogonal components even under high Fe-substitution content at the Mn site.[40] Interestingly, sign reversal of the linear ME coefficient was observed in $Mn_2Mo_3O_8$, which can be significantly magnified by Fe-substitution. Chang *et al.* studied $(Mn_{1-x}Co_x)_2Mo_3O_8$ and found that Co-doping significantly modulates magnetic interactions,[72] resulting in an FRM-to-AFM phase transition at $x = 0.35$. In samples with an FRM state ($0 \leq x \leq 0.3$), square-like magnetic hysteresis loops were observed, with remanent magnetization and coercive field strongly influenced by Co content and T.

$Ni_2Mo_3O_8$ is a spin-1 honeycomb antiferromagnet. High magnetic field measurements on single crystals of $Ni_2Mo_3O_8$ reveal two metamagnetic transitions and notable ME responses.[42] A spontaneous P emerges along the c-axis at the AFM transition $T_N \sim 5.5$ K, indicating its spin origin. This is in agreement with a remarkable ME response with H applied along the c-axis and the a-axis. In the low-H region, a weak spin-flop metamagnetic transition led to a parabolic $P(H)$ dependence. In the high-H region, a linear ME effect is observed with a relatively large $\alpha \sim 70$ ps/m. The physical essence of the spin current mechanism resides in the fact that a spin current (with spin polarization $S_i \times S_j$) flowing between two magnetic sites induces a polarization under the influence of spin–orbit coupling.[1,65] Through an analysis of the local ME tensor in $Ni_2Mo_3O_8$, both the spin current and p–d hybridization mechanisms can be applied to explain the spontaneous electric polarization and ME responses.

2.4. Corundum-related compound Ni_3TeO_6

The polar antiferromagnet Ni_3TeO_6 has attracted considerable interest due to its nonhysteretic magnetoelectricity associated with collinear AFM order. The regulatory principles governing its linear ME effect not only expand the diversity of structural types in ME materials, but also provide essential guidance for the design of ME materials within the corundum structural system, thereby advancing the research framework of linear ME materials across different structural systems.[73] The H-induced P arises along the c axis. When H exceeds a critical value H_{cri}, $P(H)$ exhibits a linear ME effect with a coefficient of -60 ps/m, consistent with the large transverse magnetic susceptibility characteristic of collinear antiferromagnets [Fig. 4(a)]. More importantly, Ni_3TeO_6 shows no hysteresis during ME switching, with a nearly flat potential barrier between the two magnetic states near the spin-flip transition [Fig. 4(b)]. This allows for continuous switching of different ME states through an intermediate state with small changes in E or H, resulting in a colossal ME response near the spin-flip transition. This resembles the large piezoelectric effect observed at morphotropic phase boundaries in ferroelectrics, offering a pathway for robust, hysteresis-free switching.

The linear ME coefficient α can be remarkably enhanced by Co-substitution in Ni_3TeO_6.[43] As shown in Figs. 4(c) and 4(d), the electric polarization (P_c) values of Ni_2CoTeO_6 and $NiCo_2TeO_6$ were measured at various temperatures, revealing a significantly enhanced ME response. In $NiCo_2TeO_6$, a large P_c of up to approximately 5200 $\mu C/m^2$ was observed under H perpendicular to the c-axis, with its value exceeding that of the parent compound. This result demonstrates the significant impact of chemical doping on enhancing the ME effect in Ni_3TeO_6 [Fig. 4(e)]. More importantly, a giant α of ~ 323 ps/m was found at $T \sim 45$ K, which greatly exceeds the conventional linear ME coefficient in Cr_2O_3, reported to be 4.2 ps/m [Fig. 4(f)]. This markedly enhanced ME response was attributed to the different occupations of Ni/Co ions at specific lattice sites. For Mn-substitution at the Ni-site, no such striking enhancement in α was observed.[74]

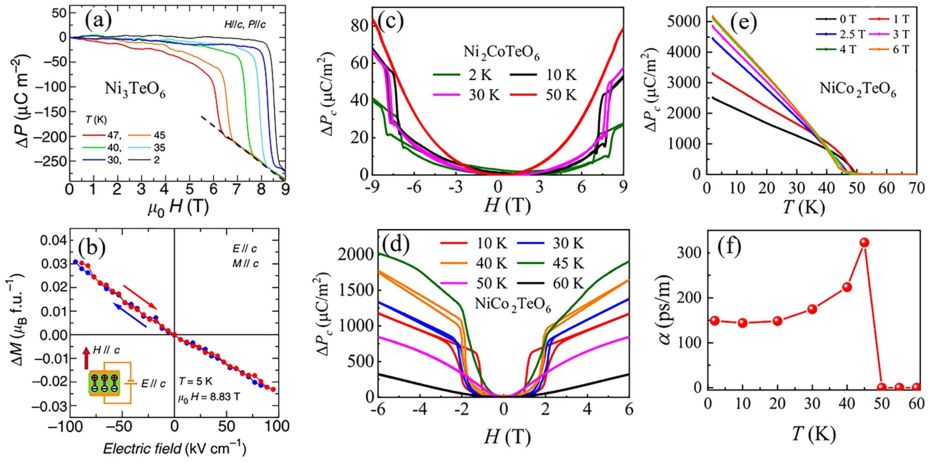


Fig. 4. (a) The P-dependence on H at different temperatures in Ni_3TeO_6. (b) Averaged $M(E)$ curve of Ni_3TeO_6. The inset shows the directions of applied magnetic field, electric field and P.[73] H-dependent P_c at different temperatures for (c) Ni_2CoTeO_6 and (d) $NiCo_2TeO_6$. (e) T-dependent of P for $NiCo_2TeO_6$ under different magnetic fields. (f) T-dependent ME coupling coefficients α of $NiCo_2TeO_6$.[43]

2.5. Other linear ME materials

Beyond these specific classes, many more linear ME materials have been synthesized. This not only refines the existing system but also opens avenues for discovering novel ME coupling mechanisms and overcoming performance limitations. $Mn_3Ta_2O_8$, an anion-deficient fluorite derivative, was identified as a linear ME material by Kimura *et al.*[12] $Mn_3Ta_2O_8$ is a rare material exhibiting both linear ME below $T_N \sim 24$ K and antiferroelectric-like orders below $T_S \sim 55$ K. The antiferroelectric phase was ascribed to the off-center displacement of magnetic Mn^{2+} ions.

Polycrystalline scheelite-type $DyCrO_4$ was synthesized under high pressure by Long *et al.*, and the ME property was extensively studied.[44,75] This material exhibits a very complex ME effect. For instance, a linear ME effect of $\alpha \sim 50$ ps/m was noted at $T = 20$ K, while a nonlinear ME effect was observed at $T = 2$ K. Single crystal samples are desired to obtain a comprehensive understanding of the ME behaviors in scheelite-type $DyCrO_4$.

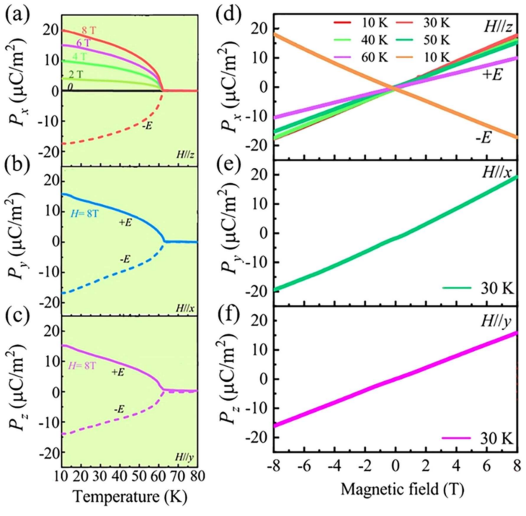


Fig. 5. T-dependence of (a) P_x, P_y, and P_z under H along the (a) z, (b) x, and (c) y directions at selected H, respectively. H -dependence of (d) P_x ($H||z$), (e) P_y ($H||x$), and (f) P_z ($H||y$) at selected T, respectively.[45]

The three-dimensional antiferromagnet Cu_3TeO_6, with cubic symmetry, has garnered attention for the coexistence of Dirac and triply degenerate magnons.[45] Induced P appears along the x-, y-, and z-axes below $T_N \sim 61$ K. The induced P can be fully reversed by opposing H, indicating intrinsic coupling between magnetism and ferroelectricity in this cubic lattice [Figs. 5(a)–5(c)]. At a selected temperature, measurements of the field-induced polarization ΔP_x, ΔP_y and ΔP_z under $H||z$, $H||x$ and $H||y$ show that the polarization increases linearly up to ~ 18 μ C/m^2, and can be reversed by an opposite electric field. This confirms a linear ME effect in Cu_3TeO_6, with ME coefficients $\alpha_{xz} \approx \alpha_{yx} \approx \alpha_{zy} = 3.1$ ps/m [Figs. 5(d)–5(f)].

3. Topological magnetoelectricity

Topology, as a concept of pure mathematics, has been widely applied to describe and illustrate many fascinating physical phenomena, such as topological insulators/semimetals/superconductors, etc.[76–78] Indeed, topology is not limited to the nontrivial electron, phonon, or photon bands in momentum space. Topological ferroic textures in real space, as an important branch of topological physics, have recently received considerable attention in condensed matter physics due to their fascinating physics and potential applications.[19,21,23,79] The magnetic skyrmion is considered as one of the most representative examples; it is a vortex-like quasiparticle at the nanometer scale. Furthermore, these topologically protected quasiparticles have been observed in some metallic systems including $Fe_{1-x}Co_xSi$, MnSi, and PdFe by means of microscopy measurement techniques.[21,79,80] Intriguingly, they can be created and annihilated utilizing electric currents. Additionally, skyrmions have also been identified in insulating chiral-lattice magnets, such as Cu_2OSeO_3 and GaV_4S_8.[80–82] Notably, both Cu_2OSeO_3 and GaV_4S_8 are multiferroics. Another famous example is the ferroelectric vortex domains in hexagonal manganite $YMnO_3$, which

are characterized by a conductive cloverleaf pattern of six antiphase domains emerging from one central point.[19,83,84] Their topological invariants can be defined by the winding number of the spin configuration or electrical dipole orientations in real space. It is worth noting that topological materials with real-space textures, such as magnetic skyrmions and ferroelectric vortex domains, exhibit trivial band structures. This is in stark contrast to topological band structures in momentum space. In addition, the real-space topological structures seem to have little link to the ME response. For example, the vortex domains in hexagonal manganites primarily represent ferroelectric polarization;[19] magnetic skyrmions in Cu_2OSeO_3/GaV_4S_8 can induce ME coupling, although it is extremely weak.[85,86]

3.1. Topological spin winding in $GdMn_2O_5$

Recently, the third type of topological physics, i.e., topological functions in ME phase space, was reported by several research groups.[24–27,87] It was found that the ME switching trajectory can surprisingly be topologically nontrivial in multiferroics. As a prototypical example, the topologically protected ME switching was first found in $GdMn_2O_5$.[24] This fascinating phenomenon is attributed to its unique crystal and magnetic structure. Figure 6(a) shows the crystalline structure of $GdMn_2O_5$.[88] In the *ab* plane, octahedrally coordinated Mn^{4+} ions and pyramidally coordinated Mn^{3+} ions are ordered in a zigzag chain along *a* with AFM intrachain exchange interactions (J_4 and J_5) between Mn spins.[89,90] Along the zigzag chain in the *b* direction, the exchange interaction J_3 between Mn^{4+} and Mn^{3+} is relatively weak. Moreover, it is geometrically frustrated due to the formation of AFM pentagons involving the neighboring Mn chains (L_1 and L_2). Rare-earth ion Gd^{3+} is embraced by the pentagonal network of Mn^{4+} and Mn^{3+} ions.

Below the ferroelectric Curie temperature of $T_C \sim 33$ K, one of the largest magnetically induced electric polarizations of 0.36 μC/cm^{-2} is identified along the *b*-axis, stemming from the Heisenberg exchange striction on both Mn^{4+}–Mn^{3+} and Mn^{4+}–Gd^{3+} bonds.[91] It is worth noting that the external magnetic field is quite efficient in tuning the ferroelectricity of $GdMn_2O_5$. When a magnetic field exceeding 5 T is applied along the *a*-axis, a pronounced polarization variation of up to 0.5 μC/cm^{-2} occurs at 2 K.[91] In addition, some prominent magnetoelectric anomalies are also observed in the cases of $H||b$ and $H||c$, i.e., this system is highly sensitive to the direction and strength of the magnetic field.[92,93] Very recently, Ponet *et al.* conducted systematic polarization measurements with the magnetic field tilted away from the *a*-axis in the *ab*-plane.[24] They found that four distinct magnetic configurations can be visited by performing two cycles of the magnetic field. Intriguingly, this ME response is merely observed within a range of the magnetic field tilted away from the *a*-axis of around 10° in the *ab*-plane, defined as the magic angle. When the magnetic field is swept up and down twice at the magic angle, the system cycles unidirectionally between four different topological magnetoelectric states, i.e., two low-field states 1 and 3 and two high-field ones 2 and 4 [Fig. 6(b)]. It is attributed to the various responses of Mn ions from zigzag chains (L_1 and L_2) to the magnetic field [Fig. 6(a)]. Namely, half of the Mn spins (L_1) perform a full 360° unidirectional rotation in approximately 90° steps, and the other half (L_2) toggle between two magnetic configurations during the field sweeps [see the middle panel of Fig. 6(c)]. As a result, they lead to the reversal of the electric polarization together based on the symmetric exchange striction (ES) mechanism triggered by the Heisenberg exchange interaction. Importantly, this magnetoelectric switching trajectory can be defined as a topological winding number $Q = 1$ (topological invariant), which describes the evolution of the Mn spin texture in the phase space. However, when the angle is smaller than the magic angle, a two-state cycle with a polarization reversal is observable, which is characterized by $Q = 0$ [see the left panel of Fig. 6(c)]. For a tilted magnetic field exceeding the magic angle, a two-state switch with $Q = 0$ occurs, which does not involve the reversal of the electric polarization [see the right panel of Fig. 6(c)]. Consequently, the distinction between the two-state switching mechanisms underpins the stability of the four-state switching behavior. It is worth mentioning that the topological magnetoelectricity of $GdMn_2O_5$ is quite fragile; e.g., the four-state cycle with polarization reversals disappears at a sample temperature above 5 K and is limited to the range of the magic angle. In addition, the research group considered that this effect was analogous to a microscopic crankshaft at the quantum level, converting linear changes of the magnetic field into a rotation of spins.

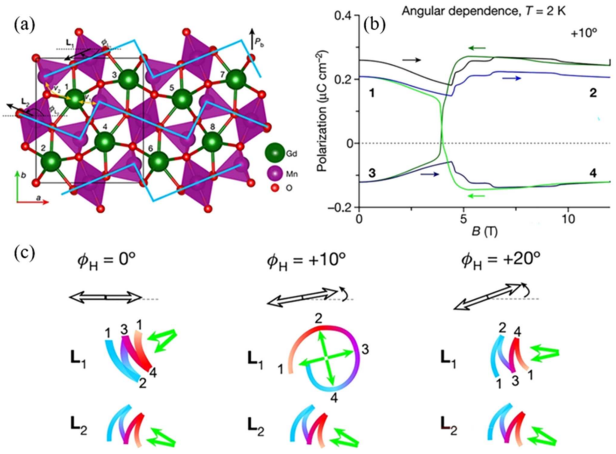


Fig. 6. (a) Crystal structure of $GdMn_2O_5$ projected in the *ab* plane. Solid cyan lines denote the zigzag chain along the *a* axis with antiferromagnetic intrachain interactions between Mn ions. (b) Evolution of ME states at the magic angle measured at 2 K. The labels 1–4 mark the four ME states. (c) For various magnetic fields tilted away from the *a*-axis in the *ab*-plane, the evolution of Mn spins at L_1 and L_2.[24]

Indeed, a closer look at the ME states of $GdMn_2O_5$ reveals that states 1 and 3 (2 and 4) are linked by space inversion symmetry. Consequently, it is natural to expect a more stable topological ME behavior by introducing an additional electric field E, which could engineer the potential energy surface to lift the degeneracy of the ME states. Inspired by the inverse ME effect, Lu *et al.* incorporated E to tune the ME states of $GdMn_2O_5$.[25] As expected, the orientation of H is not restricted to the magic angle, and the topological ME switching remains stable up to the ferroelectric Curie temperature $T_C \sim 33$ K. Compared with a pure H-cycle operation, the synchronous H–E-cycle operation can control the rotational direction of Mn spins. For example, for $H||a$, the trajectory 1–4–3–2–1 ($Q = -1$) is accomplished by adjusting the sign of E at $H = 0$ [Figs. 7(a) and 7(b)], and the trajectory 1–2–3–4–1 ($Q = 1$) is realized by reversing the polarity of E at the maximum magnetic field H_{max} [Figs. 7(c) and 7(d)]. Furthermore, simulations using the steepest descent method reveal the important effect of E in tuning the free energy landscape. In addition, multiple experiments were also carried out on other RMn_2O_5 systems (R = Dy, Er, Bi, and Y) for comparison. It is found that the 4f moment plays a crucial role in flattening the energy barriers.

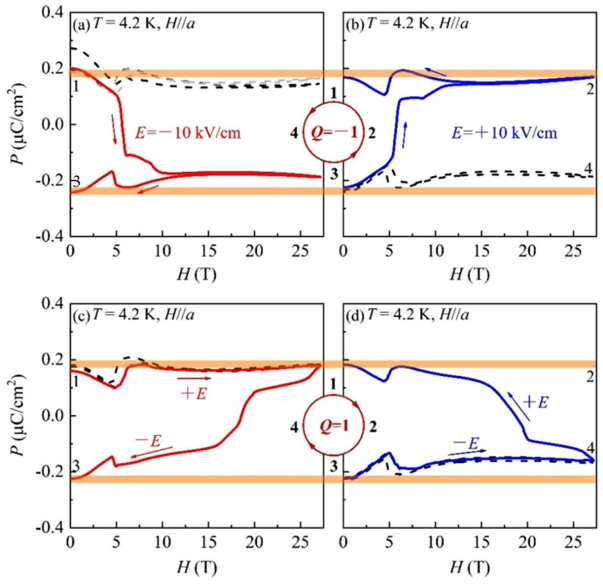


Fig. 7. Field dependence of P along the b axis measured at 4.2 K under various E. (a) The cycle (red) starting from state 1 under $E = -10$ kV/cm. (b) The following cycle (blue) starting from state 3 under $E = +10$ kV/cm. (c) The cycle (red) starting from state 1. The electric field is reversed from $+E$ to $-E$ at H_{max}. (d) The following cycle (blue) starting from state 3. The electric field is reversed from $-E$ to $+E$ at H_{max}. Q denotes the topological winding number.[25]

3.2. Roman surface topology in $RMn_3Cr_4O_{12}$

In algebraic topology, 2D topological manifolds fall into two categories: orientable and non-orientable. The former, with two sides, includes the torus and sphere. The latter, with only one side, is exemplified by the Möbius strip, Klein bottle, and Roman surface.[26] As the simplest non-orientable 2D manifold without a boundary, the Roman surface possesses several obvious features. First, its geometric topology can be represented by the different topological invariant orientability number ω because it is constituted of a Möbius strip sewed to the edge of a disk, i.e., $\omega = 0$ (orientable surface) and $\omega = 1$ (non-orientable surface).[87] Second, the mathematical equation of the Roman surface RP^2 (real projective plane) can be written as $x^2y^2 + x^2z^2 + y^2z^2 - \delta xyz = 0$, where δ is a constant and (x, y, z) is a point in Cartesian coordinates.[26] It is possible that the physical system described by the above equation realizes a Roman surface and shows a trajectory-dependent physical property. Third, its 3D realization preserves a very high tetrahedral T_d symmetry, which is characterized by four threefold symmetry axes, one triple point, six pinch points, and three self-intersecting double lines (D_a, D_b, D_c).[26] As a result, magnetoelectric multiferroics with high cubic symmetry may serve as optimal candidates for realizing the Roman surface related to topological magnetoelectricity.

Recently, a topologically non-orientable Roman surface was proposed by Long *et al.*, describing a 3D trajectory of spin-induced polarization in multiferroic $RMn_3Cr_4O_{12}$ (R = La, Tb).[26] Namely, the smooth and global evolution of electric polarization forms a non-orientable 2D manifold — a Roman surface — which is driven by the rotation of spins on the surface of a sphere [Figs. 8(a) and 8(b)]. The representative compound $TbMn_3Cr_4O_{12}$ with the $Im\bar{3}$ space group crystallizes in an A-site ordered quadruple perovskite structure with high lattice symmetry.[94,95] In contrast to the ideal perovskite structure, the Tb : Mn = 1 : 3 cation ordering yields square-planar MnO_4 units and tilted CrO_6 octahedra.[96,97] At low temperature, a high-order spin-induced ferroelectric polarization occurs along the [111] direction on the basis of the anisotropic symmetric exchange mechanism.[26,87] When rotating the spin orientations of Mn^{3+} and Cr^{3+} spins by a magnetic field, a non-trivial trajectory of the P vector is plotted on the Roman surface. This is considered as a path-dependent ME coupling effect. Figures 8(c)–8(f) show the evolution of the electric polarization in $TbMn_3Cr_4O_{12}$ as a function of the strength and angle of the magnetic field. In algebraic topology, the Roman surface is constituted by a Möbius strip sewn to the edge of a disc. As the evolution path follows the Möbius strip of the Roman surface, the rotational period of the electric polarization is half that of the magnetic field. Experimentally, while the magnetic field completes a full 360° unidirectional rotation, the electric polarization traverses the Roman surface twice [Fig. 8(e)]. By contrast, when the path falls on the orientable disk region, the rotational period of the electric polarization equals that of the magnetic field [Fig. 8(f)]. This study provides a unique perspective for deepening the understanding of the path-dependent topological ME effect in the

phase space. However, it should be noted that the aforementioned research on topological magnetoelectricity still exhibits certain limitations based on polycrystalline specimens. Afterwards, Dong *et al.* strengthened the evidence for the Roman-surface topological magnetoelectricity by using density functional theory calculations (DFT).[87] In addition, they also predicted the Roman surface topology in another quadruple perovskite, $BaMn_3Re_4O_{12}$. This prediction further expands the scope of materials exhibiting such unique topological magnetoelectricity.

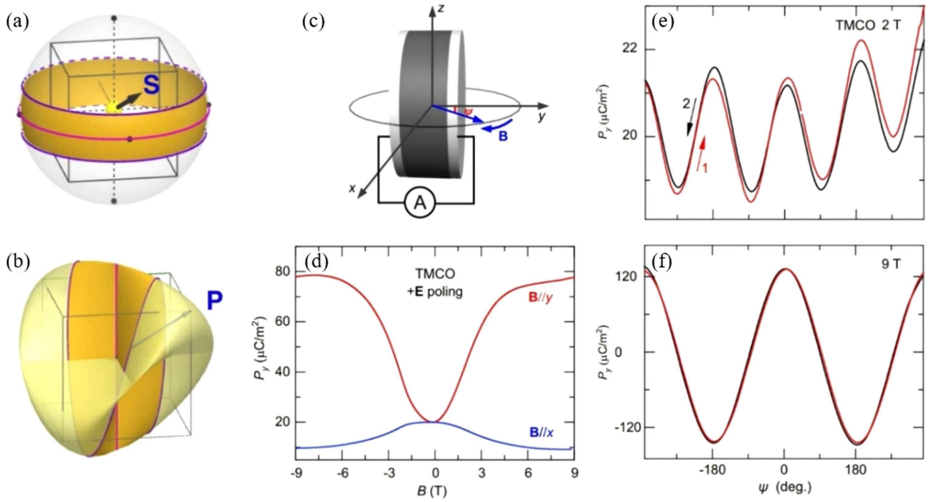


Fig. 8. (a) and (b) Loops of the sphere of Néel vectors (upper panels) and the correspondingly induced polarization trajectories on Roman surface (bottom panels). (c) Measurement geometry for ME current under rotating magnetic field. (d) Electric polarization dependence of H measured at 10 K. (e) and (f) At different strengths of H, electric polarization dependence of the rotational angle of H measured at 10 K.[26]

3.3. Double-leaf Riemann surface topology in GdI_2

In 2024, Dong *et al.* proposed another type of topological magnetoelectricity, coined as the double-leaf Riemann surface, on the basis of theoretical calculations.[27] The ferromagnetic GdI_2 monolayer serves as the model system to demonstrate the unique functional relationship between spins and polarizations. Unlike the van der Waals bulk GdI_2 with a centrosymmetric structure, the monolayer GdI_2 (space group $P\bar{6}m2$) is noncentrosymmetric and adopts the honeycomb structure.[27] In this structure, Gd^{2+} ($4f^75d^1$) sits at the center of the trigonal prism.[98] Due to the distorted trigonal prism, the 5d electron occupies a singlet orbital, which is a hybrid of the $3z^2 - r^2/x^2 - y^2/xy$ orbitals.[99] This situation results in an easy-plane magnetocrystalline anisotropy according to first-principles calculations. Based on the orientation of the magnetic moments, the magnetic point group of the GdI_2 monolayer can become polar. Hence, the ferroelectric polarization can be driven by the spins, which originates from the mechanism of spin-dependent p–d hybridization.[27] Namely, the monolayer GdI_2 hosts intrinsic magnetoelectricity that refers to the tunability of magnetism (ferroelectricity) via an electric (a magnetic) field. When the *ab*-plane magnetic field undergoes a full 360° unidirectional rotation, the spin-induced polarization of the GdI_2 monolayer rotates two turns [Fig. 9(a)]. Conversely, when the *ab*-plane electric field undergoes two continuous cycles, the spin of the Gd ions returns to its original configuration [Fig. 9(b)]. In other words, one cycle of rotation of the electric field results in the reversal of electric polarization. Intriguingly, the nontrivial control of magnetization can be realized using an *ac* electric field in such topological magnetoelectricity, which could be designed to process information reading/writing in future spintronic devices. Figure 9(c) summarizes the coupled relationship between the electric and magnetic degrees of freedom in GdI_2, i.e., a ratio of 1:2, which forms a topological double-leaf Riemann surface. The analytical formula of the double-leaf Riemann surface obeys $(\boldsymbol{S}\cdot\boldsymbol{e})^2$ in mathematics. According to symmetry classification of two-dimensional noncentrosymmetric point groups, the double-leaf Riemann

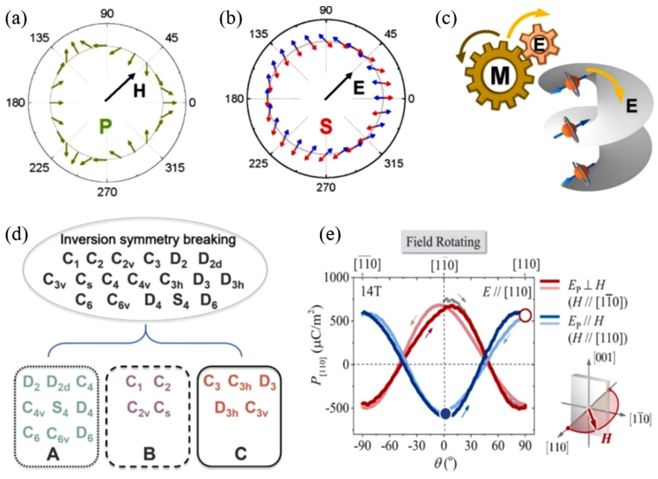


Fig. 9. (a) Evolution of electric polarization upon the rotation of *ab*-plane magnetic field. (b) Evolution of Gd spin upon the rotation of *ab*-plane electric field. (c) Schematic illustrations of topologic double-leaf Riemann surface. (d) Symmetry classification and more candidates for the double-leaf Riemann surface topological magnetoelectricity. (e) In $Co_4Nb_2O_9$, the dependence of electric polarization on angle θ defined by the relative direction of the magnetic field.[27,100]

surface topological magnetoelectricity is expected to be found in material systems with point groups in classes B and C [Fig. 9(d)]. Moreover, it allows the dissipationless converse magnetoelectricity for those point groups in class C. Note that the GdI_2 monolayer has not yet been experimentally exfoliated from the bulk, so the aforementioned prediction remains to be verified. Indeed, Khanh *et al*. has observed a similar magnetoelectric phenomena in a honeycomb antiferromagnet $Co_4Nb_2O_9$.[100] The direction of spin-induced polarization is reversed by rotating the magnetic field of 90° [Fig. 9(e)]. Certainly, whether this magnetoelectric feature corresponds to topological double-leaf Riemann surface requires further investigation.

4. The 2D multiferroics

The 2D systems can host emergent effects absent in conventional bulk materials, giving rise to rich new physical phenomena. Yet, conventional ferroelectric and ferromagnetic thin films often face challenges such as quantum tunneling, dangling bonds, and depolarization effects, which hinder their stability at the nanoscale.[101] The rise of 2D van der Waals (vdW) materials has provided a promising pathway to overcome these limitations. Owing to their dangling-bond-free surfaces and saturated in-plane chemical bonds, 2D layered materials exhibit excellent structural stability down to the monolayer limit, while allowing flexible tuning of ferroic phases through thickness, stacking, external fields, and interface engineering.[30] In recent years, intensive studies on graphene have significantly advanced the characterization and modeling techniques of 2D materials.[102,103] Building upon these developments, researchers have begun to apply cutting-edge theoretical and experimental approaches to 2D multiferroics, leading to the identification of a number of systems. These include intrinsic 2D multiferroics (e.g., NiI_2,[104] $CuCrP_2S_6$,[105] and $Hf_2VC_2F_2$,[106] etc.) as well as a variety of artificially engineered multiferroic structures. These systems offer an ideal platform for investigating ferroic orders and coupling mechanisms, and hold great promise for applications in high-density memory, energy conversion, and multifunctional nanoelectronics. In the following, we highlight key features of 2D multiferroics through representative systems.

4.1. Intrinsic 2D multiferroic materials

Intrinsic 2D multiferroic materials refer to ones whose ferroic orders arise from the materials' inherent structure and symmetries. The multiferroic NiI_2 is popular among 2D vdW materials. It has been proven to host a type-II multiferroic ground state. As the temperature decreases, NiI_2 transitions from a paramagnetic state to an antiferromagnetic state at 76 K and further transforms into a helimagnetic state at 60 K, accompanied by a structural transition. At room temperature, bulk NiI_2 crystallizes in the rhombohedral $R\bar{3}m$ structure [Fig. 10(a)]. In the helimagnetic ground state, ferroelectricity in NiI_2 originates from the breaking of inversion symmetry by the spin spiral state, which was probed by polarization current measurements under a [1, –1, 0] oriented in-plane magnetic field, confirming in-plane [1, 1, 0] polarization.[107] By using mechanical exfoliation to obtain bilayer flakes of NiI_2 and employing optical second-harmonic generation (SHG) techniques, Ju *et al*. revealed that the multiferroic state persists down to the bilayer limit of NiI_2 and the transition temperature decreases from 58 K in bulk to approximately 20 K in the bilayer.[108]

To obtain monolayer NiI_2, NiI_2 flakes were grown by physical vapor deposition (PVD) and subsequently transferred onto a SiN_x membrane using the dry transfer technique by Song *et al*.[104] One- and two-layer NiI_2 crystals were grown by PVD on hexagonal boron nitride. Circular dichroic Raman, birefringence, and second-harmonic generation measurements were then used, combined with theoretical modeling and simulations, to reveal that multiferroicity persists down to the 2D limit in monolayer NiI_2 [Figs. 10(b) and 10(c)].[109] The transition temperatures of 21 K (monolayer), 30 K (bilayer), 39 K (trilayer), and 41 K (four-layer) align closely with subsequent theoretical calculations and other reported measurements.

However, some doubted that all optical measurements may not be sufficient to prove the existence of ferroelectricity.[110] In their opinion, the optical signals may exclusively stem from the breaking of spatial-inversion or time-reversal symmetry induced by magnetic order. Later, some other researchers sought other ways to prove the existence of ferroelectricity. Some probed and characterized the multiferroic order in monolayer NiI_2 at the atomic scale and investigated its ME coupling by manipulating multiferroic domains through scanning tunneling microscopy (STM) tip-induced local electric fields.[111] Another group of researchers conducted magneto-optical-electric joint measurements and observed the coexistence of ferroelectricity and antiferroelectricity.[112] In addition, computational studies attribute the multiferroic behavior in monolayer NiI_2 to the interplay of spin-spiral order and spin–orbit coupling.[111]

Skyrmions along with their potential topological properties have also been found in NiI_2. Density functional theory and Monte Carlo simulations indicate that monolayer NiI_2 exhibits a triple-q state below T_C, at approximately 30 K.[113] This state hosts a spontaneous antibiskyrmion lattice with a topological charge of $|Q| = 2$. Additionally, an applied magnetic field can induce a transition to a Bloch-type skyrmion lattice. The common origins of skyrmions are the Dzyaloshinskii–Moriya (DM) interaction and long-ranged interactions causing magnetic frustration. However, the spon-

taneous skyrmionic state in NiI_2 is different; it can be driven only by the anisotropic component of the short-range symmetric exchange, without DM and Zeeman interactions. It is novel and significant to observe topological properties in 2D multiferroics, though experimental confirmation has been absent to date.

Simultaneously, studies exploring other aspects of NiI_2: Song *et al*. transferred a 20-nm-thick NiI_2 flake between two gold electrodes [Fig. 10(d)].[109] Subsequently, the photocurrent from the bulk photovoltaic effect was measured during the heating process using photoexcitation [Fig. 10(e)]. They found that the spin chirality in NiI_2 can be reversed by switching the spin-induced ferroelectric polarization, which was supported by group theory analysis and DFT calculations. Pressure,[114] sliding, and twisting in bilayer[35] are also in progress. These investigations not only demonstrate the typical properties of NiI_2 as a 2D multiferroic, but also show its exceptional potential for spintronic devices.

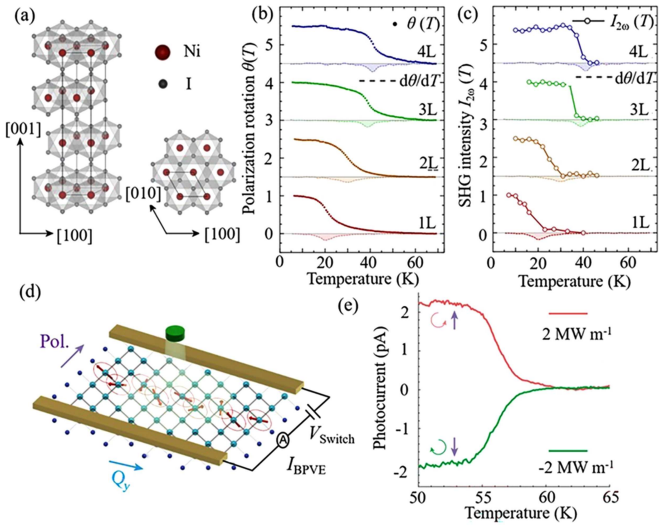


Fig. 10. Structure of bulk NiI_2, optical evidence of monolayer multiferroics and photocurrent measurements. (a) The structure of bulk NiI_2 at room temperature. (b) and (c) Measurements of temperature-dependent, birefringence-induced polarization rotation and electric-dipole second harmonic generation intensity from monolayer to four-layer.[104] (d) Schematics of zero-bias photocurrent measurement. (e) Temperature-dependent zero-bias photocurrent measurement in a 20-nm-thick NiI_2 flake.[109]

Unlike NiI_2, $CuMP_2X_6$ (M = Cr, V; X = S, Se) is a type-I multiferroic. By using first-principles density functional theory, Qi *et al*. demonstrated the coexistence of ferromagnetism and ferroelectricity in monolayer transition metal phosphorus chalcogenides $CuMP_2X_6$ (M = Cr, V; X = S, Se).[115] $CuMP_2X_6$ are layered van der Waals materials which had been experimentally synthesized in the 1990s. In the paraelectric phase, both Cu and Cr/V atoms are in the middle plane while in the ferroelectric phase, the displacement of the Cu atoms along the direction normal to the plane results in spontaneous out-of-plane polarization. Calculations showed that applying an external electric field allows for control of the ferroelectric-paraelectric phase transition. Regarding the magnetic properties, the spin density distribution in the ferromagnetic state of monolayer $CuCrP_2S_6$ indicated that the magnetic moments are primarily localized at the Cr/V atoms. Furthermore, the ferromagnetic order arises from the indirect exchange mechanism between Cr/V atoms which is mediated by the Cu and S/Se atoms.

Ferromagnetism and out-of-plane ferroelectricity have been experimentally observed in the 2D van der Waals material $CuCrP_2S_6$.[105] $CuCrP_2S_6$ flakes were synthesized and then exfoliated into nanosheets. Figure 11(a) presents an atomic force microscopy image of a $CuCrP_2S_6$ nanosheet with a thickness of about 13.3 nm. Researchers used piezo force microscopy to characterize the ferroelectricity of $CuCrP_2S_6$ nanosheets. Figure 11(b) presents the hysteresis loop of phase and curves of polarized amplitude versus DC bias voltage. The hysteresis loop shows little sign of degradation after multiple measurement cycles. As shown in Fig. 11(c), this robustness confirms the sustainable ferroelectricity of $CuCrP_2S_6$, demonstrating it as a 2D ferroelectric material. Regarding the magnetic properties, the bulk sample ($\sim$ 1 μm thick) exhibits no magnetic hysteresis. In contrast, the material shows intrinsic in-plane ferromagnetism after reducing the thickness. The temperature-dependent magnetization and the magnetic hysteresis loop were measured at 10 K [Figs. 11(d) and 11(e)]. These results collectively confirm the emergence of robust ferromagnetism in few-layer $CuCrP_2S_6$. Meanwhile, studies have revealed in-plane anisotropy in van der Waals multiferroic $CuCrP_2S_6$, which is believed to play a critical role in the ME coupling.[116]

It has been proposed that 2D $MoPtGe_2S_6$, a material predicted to be intrinsically multiferroic but not yet synthesized, could form a vdW multiferroic tunnel junction (MFTJ) in a bilayer configuration and exhibit six resistance states under different conditions.[117] In monolayer $MoPtGe_2S_6$, ferroelectricity originates from the migration of Ge–Ge atomic pairs along the z-axis, and magnetism derives from Mo atoms, together giving rise to multiferroicity. Researchers proposed a vdW MFTJ consisting of bilayer $MoPtGe_2S_6$ and symmetric $PtTe_2$ electrodes, with each monolayer exhibiting intrinsic multiferroicity. First-principles calculations show that by tuning ferroelectric and ferromagnetic polarization directions, this MFTJ can achieve six distinct non-volatile resistance states, with high tunneling magnetoresistance (TMR) and electroresistance (TER) ratios. Furthermore, the MFTJ exhibits remarkable spin-filtering and a significant negative differential resistance effect, making it a promising candidate for advanced spintronic devices.

MXenes are a class of 2D transition metal carbides and carbonitrides. Their chemical composition is given by the formula: $M_{n+1}X_nT_x$, where M represents an early transition metal,

X is carbon or nitrogen, and T represents F, O, or OH. Derived from an experimental $Hf_3C_2T_x$ monolayer, the ordered double transition metal carbides $Hf_2MC_2T_2$ monolayers are considered to be 2D type-II multiferroics.[106] By comparing various possible structural configurations and magnetic ground states of $Hf_2VC_2F_2$, researchers found that the AA CG configuration and the 120° noncollinear antiferromagnetic order (Y-AFM) are the most likely. Since the Y-AFM is a type of helical spin order that breaks inversion symmetry, they calculated its properties relevant to type-II multiferroicity. Subsequent calculations revealed that the estimated Néel temperature T_N reaches 313 K, which exceeds room temperature, and ferroelectricity develops below T_N with its polarization P always perpendicular to the spin helical plane. Therefore, the $Hf_2VC_2F_2$ monolayer is a type-II multiferroic at room temperature. Although researchers thought it could possibly be realized via the 3D pattern Hf_2MAlC_2, its synthesis has remained an unrealized challenge to date.

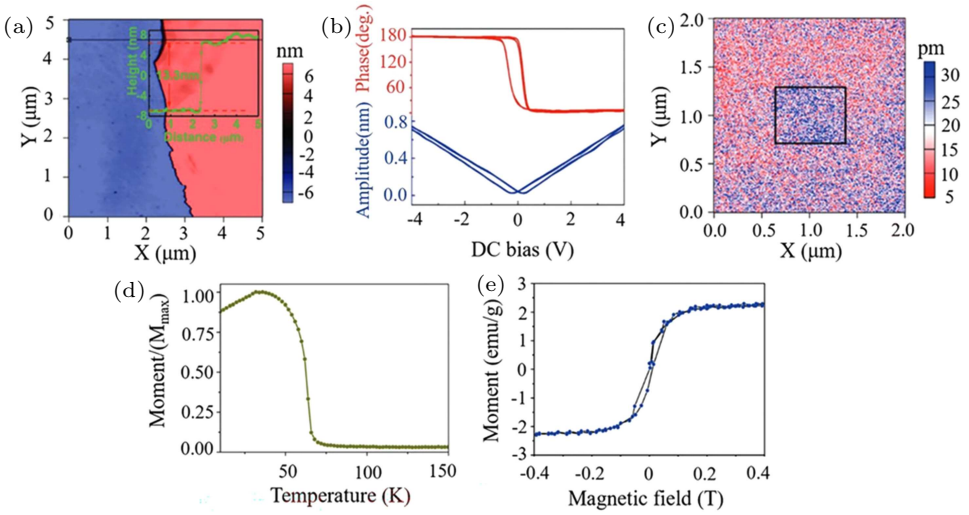


Fig. 11. Measurements of ME properties on $CuCrP_2S_6$. (a) Atomic force microscopy image of a 13.3 nm thick $CuCrP_2S_6$ nanosheet. (b) The phase-DC bias hysteresis loop and amplitude-DC bias curve. (c) Written pattern of $CuCrP_2S_6$. (d) Temperature dependence of the magnetization in $CuCrP_2S_6$. (e) Magnetic hysteresis loop of $CuCrP_2S_6$ at 10 K.[105]

The 2D organic material C_6N_8H (g-C_3N_4) has been identified as a 2D multiferroic owing to its high Curie temperature and the coupling between ferroelectricity and ferromagnetism. It is found to exhibit room-temperature ferromagnetism, which can be controlled by hydrogen concentration. Furthermore, hydrogenation induces proton-transfer ferroelectricity. Tu *et al*. found that oxygen molecules from air catalyze the long-range proton transfer by reducing its energy barrier. This effect enables switchable polarization under ambient conditions, although these theoretical predictions await experimental validation.[118]

In fact, research on 2D multiferroics remains in its infancy, especially experimentally. Although some have been theoretically predicted, very few, like NiI_2, have been successfully synthesized down to the monolayer limit. Both synthesis and characterization face significant challenges. The former requires more advanced techniques and guidance from theoretical predictions to identify efficient pathways, while in the latter, the evidence for multiferroicity is generally indirect — e.g., via optical methods — demanding more direct probing techniques. Furthermore, producing stable, high-quality, and large-scale 2D multiferroics, akin to conventional 2D materials, remains a distant goal requiring extensive effort.

4.2. Artificially engineered 2D multiferroic systems

Unlike the lattice-matching constraints of 3D materials, 2D multiferroics benefit from their inherent layered structures and weak interlayer van der Waals interactions, offering unprecedented flexibility for artificial design. For example, spontaneous ferroelectricity can be induced by external effects such as doping, intercalation, homostructure sliding, and heterostructure stacking to tune specific properties. These artificially engineered 2D multiferroic systems not only provide pathways to achieve strong and tunable ME coupling, but also enable reversible control of ferroic orders at the atomic scale. More importantly, their unique quantum effects and structural diversity endow them with enormous potential for applications in next-generation spintronics and quantum devices.

Among these strategies, electron or hole doping can directly regulate the electronic structure, charge distribution, and spin states of materials, thereby inducing ferroelectric polarization or magnetic ordering without destroying long-range order. For instance, electron doping in the magnetic monolayer $CrBr_3$ induces in-plane multiferroicity [Figs. 12(a) and 12(b)]. $CrBr_3^{x-}$ $(0 < x \leq 0.5)$ exhibits pronounced Jahn–Teller (JT) distortions, and in-plane ferroelectricity is preserved through the combined effects of charge and orbital ordering.[119] In $(CrBr_3)_2Li$, due to the asymmetric Jahn–Teller distortion of

$Cr–Br_6$ octahedral units, the magnetic coupling and electronic structure near the Fermi level, such as the splitting of Cr-e states, undergo significant changes [Fig. 12(c)], leading to the emergence of in-plane polarization.

Halogen vacancies provide an easier way to introduce ferroelectricity into FM monolayer metal trihalides. With the incorporation of I vacancies in magnetic monolayer CrI_3, not only is the intrinsic ferromagnetism of monolayer CrI_3 enhanced, but the symmetry of charge density distribution between the upper and lower surfaces is also broken, further inducing switchable polarization [Figs. 12(d) and 12(f)]. This originates from the unique porosity of CrI_3, which allows I vacancies to readily hop between the top and bottom surfaces, resulting in a moderate energy barrier for polarization switching.[120] Such two-dimensional switchable polarization induced by surface vacancies is also applicable to many other metal trihalides.

In addition, intentional doping of magnetic elements into specific regions of 2D ferroelectric semiconductors is predicted to lead to the coexistence of ferroelectric and ferromagnetic orders, akin to diluted magnetic semiconductors. A representative case is Fe-doped 2D ferroelectric In_2Se_3 ($Fe_{0.16}In_{1.84}Se_3$), in which magnetic ordering is induced [Fig. 12(g)], while its intrinsic ferroelectricity is simultaneously enhanced by magnetic ion incorporation.[121] By substituting 1/3 of Ta ions with Fe, the i-MAX phase of Ta_2C, $(Ta_{2/3}Fe_{1/3})_2C$, can be obtained. This partially ordered Fe substitution not only introduces magnetism into the system but also reduces the structural symmetry to space group $C2/m$ (No. 12), thereby breaking the in-plane threefold rotational symmetry. Furthermore, when the surface metallic layer of $(Ta_{2/3}Fe_{1/3})_2C$ is passivated with oxygen [Fig. 12(h)], p–d hybridization occurs between Fe^{2+} and Ta^{5+}, leading to structural distortions.[122] The resulting $(Ta_{2/3}Fe_{1/3})_2CO_2$ monolayer is a type-I 2D multiferroic. Its ferroelectricity originates from C/O 2p–Ta 5d orbital hybridization, while ferromagnetic order arises from the Fe sublattice. The polarization strength is moderate and remains stable above room temperature. More importantly, this system demonstrates strong ME coupling, with the Néel temperature being markedly tunable at the ferroelectric–paraelectric transition or along ferroelectric domain walls.

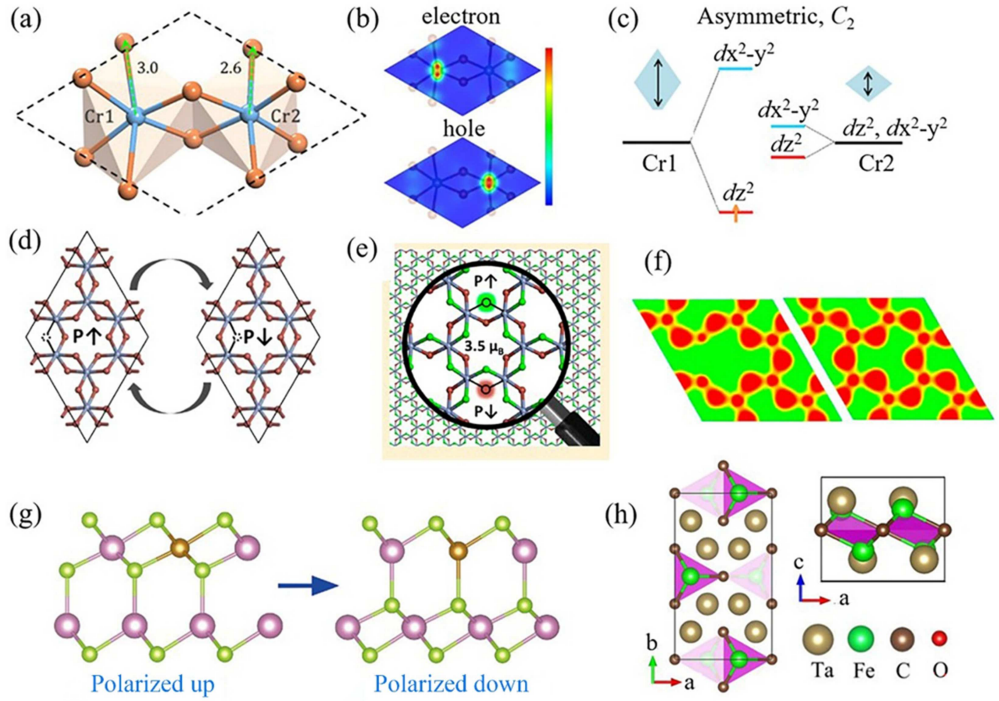


Fig. 12. (a) Optimized top view of the $CrBr_3^{0.5-}$ monolayer. (b) Real-space electron and hole density distributions at the valence-band maximum and conduction-band minimum. (c) Evolution of electronic states under asymmetric JT distortions.[119] (d)–(e) Schematic illustration of IV-CrI_3 as an atomically thin 2D system with reversible out-of-plane polarization, where vacancies are marked by black dotted circles. (f) Charge density distribution of IV-CrI_3 containing a top-layer I vacancy.[120] (g) Schematic representation of a single quintuple layer of $Fe_{0.16}In_{1.84}Se_3$ with upward and downward polarization states.[121] (h) The structure of the i-MAX phase $(Ta_{2/3}Fe_{1/3})_2C$ is depicted with the top view on the left and the side view on the right.[122]

The scarcity of single-phase multiferroic materials has also driven researchers to focus on composite systems of ferroelectrics and magnets.[4] In this context, 2D vdW materials provide notable advantages: their layered architecture enables different components to be stacked in a LEGO-like manner without significant interfacial reconstruction, thus retaining their intrinsic properties at the atomic scale. Although the interlayer mechanical coupling is relatively weak, charge redistribution or field effects can still induce multiferroicity, and related 2D heterostructures have been predicted.[123] The first two-dimensional heterostructured multiferroic was realized by combining a ferromagnetic $Cr_2Ge_2Te_6$ mono-

layer with a ferroelectric In_2Se_3 monolayer [Figs. 13(a) and 13(b)]. First-principles calculations show that the interplay of interfacial Rashba spin–orbit coupling and electronic reconstruction can modulate magnetic interactions, giving rise to magnetic phases absent in the individual layers. Reversing the polarization of In_2Se_3 can switch the magnetocrystalline anisotropy of $Cr_2Ge_2Te_6$ between an easy axis and an easy plane.[124] Moreover, this ME coupling also renders In_2Se_3 itself a switchable magnetic semiconductor. Such "dual-functional" heterostructures open a new pathway for engineering ferroic orders in 2D materials through artificial stacking. This configuration has also been extended to other magnetic 2D materials to construct all-vdW layered multiferroics, such as LaCl/α-In_2Se_3,[125] Fe_3GeTe_2/α-In_2Se_3,[126] CrI_3/α-In_2Se_3,[127] and InSe/In_2Se_3.[128] Recent studies have demonstrated that coupling 2D magnets with ferroelectric (FE) layers possessing multiple polarization states enables nonvolatile and multistate manipulation of magnetism. Using DFT and Monte Carlo simulations, novel FE materials with quadruple potential wells ($Pt_2Sn_2Se_6$, $Pt_2Sn_2Te_6$, $Pd_2Sn_2Se_6$, $Pd_2Sn_2Te_6$) were predicted, where distinct Sn pair displacements create multiple stable polarization states. When a monolayer CrI_3 is integrated with $Pt_2Sn_2Te_6$ to form a heterojunction, the system exhibits multiple magnetic phases, including ferromagnetic states, Bloch-type skyrmions, and a newly discovered topological magnetic superstructure. These states can be reversibly switched through ferroelectric polarization reversal and interlayer sliding [Figs. 13(c) and 13(d)]. The emergence of skyrmions is attributed to interfacial DM interaction consistent with the Fert–Levy mechanism.[129] Remarkably, skyrmion lattices remain stable even after removing the magnetic field, highlighting their robustness. This work underscores the potential of multiferroic heterojunctions as a platform for nonvolatile control of 2D magnetism and emergent spin textures.

Compared with 3D systems, 2D composite multiferroic materials possess greater degrees of freedom due to the absence of lattice-matching constraints. For example, multiferroicity can be achieved simply by sliding or twisting stacked magnetic monolayers. The sliding-induced mechanism allows polarization direction and magnetic states to be switched via small interlayer displacements, providing a flexible and efficient strategy for constructing tunable 2D multifunctional materials. Multilayer MnSe constructed from monolayers exhibits large out-of-plane polarization driven by sliding, accompanied by a switchable net magnetic moment [Fig. 14(b)]. Compared with conventional 2D sliding ferroelectric materials, MnSe shows stronger polarization, which can be further enhanced by increasing the number of layers, applying strain, or hole doping.[34] It simultaneously exhibits reversible ferroelectricity and magnetism with a moderate sliding energy barrier. In bilayer GdI_2, sliding ferroelectricity enables coupling among magnetic, ferroelectric, and valleytronic properties.[130] Monolayer GdI_2 is a ferromagnetic semiconductor exhibiting strong valley polarization, whereas in the bilayer, interlayer sliding enables tuning of the magnetic ground state and reversible switching of both ferroelectric and valley polarizations [Fig. 14(a)]. Studies reveal that interlayer electronic transitions are the microscopic mechanism underlying the magnetic phase transition.

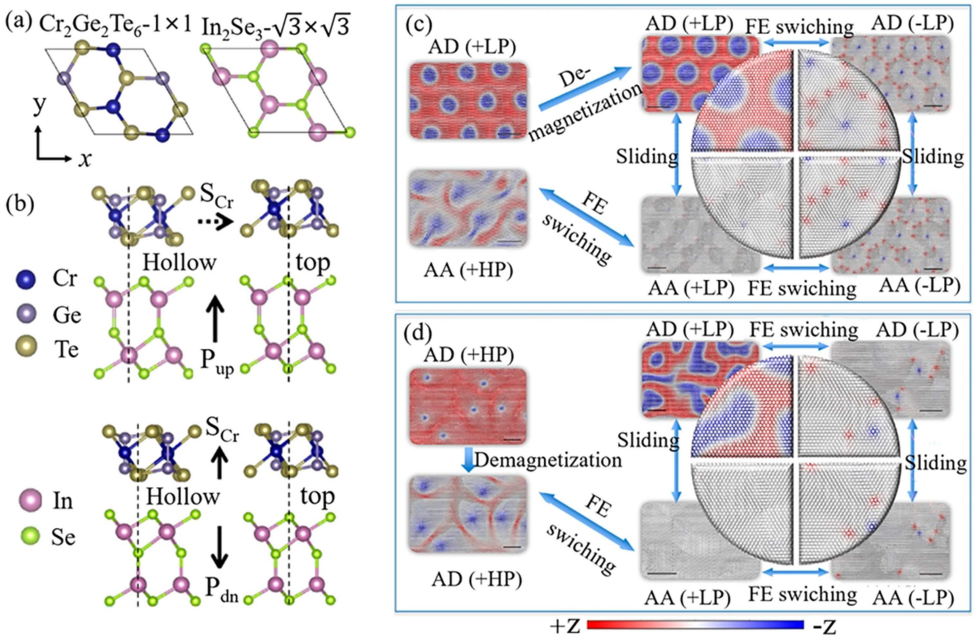


Fig. 13. (a)–(b) Side views of the heterostructure with the ferroelectric dipole moment of In_2Se_3 oriented upward and downward (P↑ and P↓).[124] (c)–(d) Reversible evolution of the magnetic configuration in the CrI_3/$Pt_2Sn_2Te_6$ heterojunction under interlayer sliding and FE polarization switching.[129]

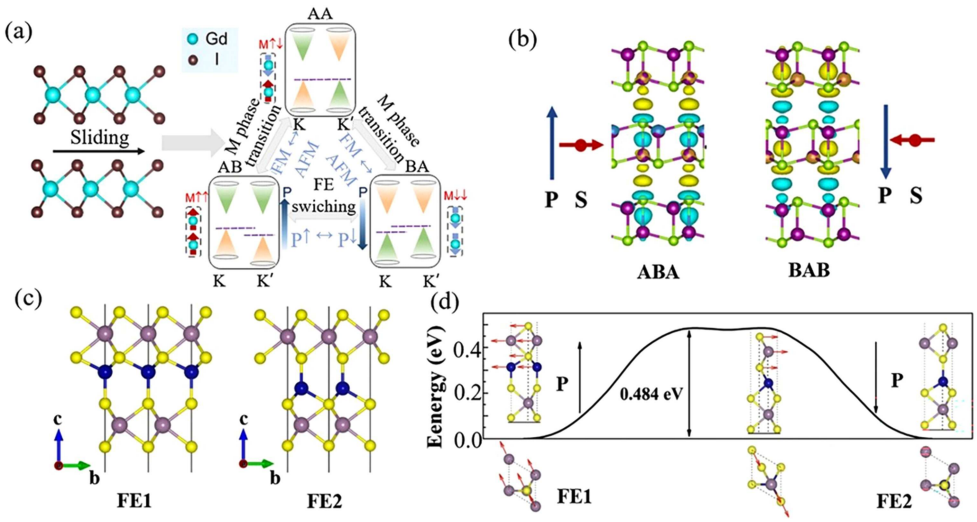


Fig. 14. (a) Illustration of the mechanism underlying the coexistence of magnetic, ferroelectric, and ferrovalley orders in GdI_2.[130] (b) Sliding ferroelectricity and magnetoelectric coupling in MnSe multilayers.[34] (c) Left and right views of the $Co(MoS_2)_2$ monolayer in the FE1 and FE2 ferroelectric phases. (d) Ferroelectric switching pathway of $Co(MoS_2)_2$ calculated using the NEB method.[132]

Twist-angle stacking can induce noncollinear spin textures, local ferroelectric polarization, and topological magnetism, providing a new avenue for realizing complex multiferroicity and topological states. CrI_3, as one of the first experimentally confirmed 2D ferromagnets, has become a model system for studying low-dimensional magnetism and multiferroicity. Its interlayer magnetic coupling is highly sensitive to stacking patterns, and sliding ferroelectricity can be induced by adjusting the stacking sequence.[31,32] These stacking-dependent multiferroic properties make twisted CrI_3 an ideal platform for studying how structural relaxation affects magnetism and ferroelectricity in moiré superlattices. First-principles studies show that spontaneous structural relaxation significantly modifies the interlayer stacking potential, suppressing the formation of magnetic bubbles in small-angle twisted bilayers, while ferroelectric vortices remain stable due to topological protection. Due to changes in interlayer exchange and anisotropy, the magnetic ground state is strongly modulated by stacking patterns and twist angles. In contrast, ferroelectric domain walls remain robust despite being compressed.[131] These results indicate that rigid-lattice models cannot fully capture the complex multiferroic behavior in twisted 2D layers; structural relaxation must be considered to accurately predict and design multiferroicity. The principles revealed in CrI_3 can be generalized to other twisted 2D systems, providing a universal framework for precise control of magnetism, ferroelectricity, and topological order through twist angle, layer thickness, and relaxation-induced stacking modulation.

Ion intercalation also provides an effective strategy to induce multiferroicity in 2D van der Waals (vdW) materials. The van der Waals gaps in these materials can be readily intercalated with atoms, molecules, or atomic layers, allowing their properties to be tuned. Recently, intercalating magnetic atoms into bilayer transition metal dichalcogenides (TMDs) has become a key approach for realizing electric-field-controllable magnetism. First-principles calculations show that nonmetallic bilayer TMDs acquire both ferroelectricity and magnetism upon transition metal ion intercalation. For example, in Co-intercalated bilayer MoS_2 [$Co(MoS_2)_2$], Co atoms introduce local magnetic moments and break interlayer symmetry to generate polarization, yielding switchable ferroelectricity. Notably, the system exhibits two degenerate ferroelectric phases (FE1 and FE2) [Figs. 14(c) and 14(e)] with opposite Dzyaloshinskii–Moriya interaction (DMI) chirality.[132] Consequently, applying a vertical electric field allows ferroelectric polarization switching to directly toggle between magnetic ground states of opposite chirality, enabling electric-field control of skyrmion chirality.

5. Summary and outlook

To summarize, we have provided a concise overview of recent progress in multiferroics. Significant advances have been achieved in understanding linear ME effects, topological magnetoelectricity, and 2D multiferroics. The linear ME effect, characterized by the mutual induction of electric polarization and magnetization, has been driven forward by advances in single-phase materials and a refined understanding of microscopic mechanisms. Topological magnetoelectricity, a novel ME coupling phenomenon, enables precise control of the states of magnetic and electric dipoles via well-defined real-space trajectories, paving the way for high-density information storage and low-power spintronic technologies. Meanwhile, progress has been made in both the theoretical prediction and experimental verification of intrinsic 2D multiferroics, while artificially engineered 2D multiferroic systems have further expanded the material library and tuning strategies.

Nevertheless, several key challenges and promising future directions remain for multiferroic and ME materials. Due to the inherent repulsion between ferroelectricity and ferromagnetism, current linear ME materials cannot achieve both room-temperature stability and strong coupling. Thus, designing novel lattice structures or composite systems offers a promising avenue to overcome this barrier. Still, both topological magnetoelectricity and 2D multiferroics remain in their infancy. Not only are the discovery and synthesis of new materials important, but also the development of more robust methods for experimental verification. The topological ME effect depends strongly on the orientation of the spin texture. Usually, it is experimentally accessible by tracking the electric-polarization path in an applied magnetic field. This effect may be characterized by recording the evolution of the sample deformation (e.g., magnetostriction) in some magnetically induced multiferroics with spin-lattice coupling. Similarly, a critical challenge in 2D multiferroics is the experimental realization of numerous predicted materials. This requires more direct probing techniques and theoretical predictions to guide efforts not only in material selection but also in identifying efficient synthetic pathways.

Additionally, exploring dynamic and ultrafast ME effects could enable high-speed applications by overcoming the speed limitations inherent in conventional electromagnetic approaches.[133,134] Meanwhile, investigating ME effects in quantum materials and low-dimensional systems may reveal novel phenomena. By addressing these frontiers, the field of linear magnetoelectricity can continue its path of fundamental discovery and technological innovation, contributing to a new era of energy-efficient multifunctional materials.

Acknowledgements

Project supported by the National Key Research and Development Program of China (Grant No. 2024YFA1611200) and the National Natural Science Foundation of China (Grant Nos. 12474085 and 12574095).

References

[1] Dong S, Liu J M, Cheong S W and Ren Z F 2015 *Adv. Phys.* **64** 519
[2] Dong S, Xiang H and Dagotto E 2019 *Natl. Sci. Rev.* **6** 629
[3] Lu C, Wu M, Lin L and Liu J M 2019 *Natl. Sci. Rev.* **6** 653
[4] Spaldin N A and Ramesh R 2019 *Nat. Mater.* **18** 203
[5] Eerenstein W, Mathur N D and Scott J F 2006 *Nature* **442** 759
[6] Tokura Y and Nagaosa N 2018 *Nat. Commun.* **9** 3740
[7] Cheong S W, Talbayev D, Kiryukhin V and Saxena A 2018 *npj Quantum Mater.* **3** 19
[8] Iyama A and Kimura T 2013 *Phys. Rev. B* **87** 180408
[9] Mukherjee S, Roy A, Auluck S, Prasad R, Gupta R and Garg A 2013 *Phys. Rev. Lett.* **111** 087601
[10] Mufti N, Blake G R, Mostovoy M, Riyadi S, Nugroho A A and Palstra T T M 2011 *Phys. Rev. B* **83** 104416
[11] Zhou G Z, Gong J W, Li X, *et al*. 2019 *Appl. Phys. Lett.* **115** 252902
[12] Kimura K, Yagi N, Hasegawa S, Hagihala M, Miyake A, Tokunaga M, Cao H, Masuda T and Kimura T 2021 *Inorg. Chem.* **60** 15078
[13] Khanh N D, Abe N, Sagayama H, Nakao A, Hanashima T, Kiyanagi R, Tokunaga Y and Arima T 2016 *Phys. Rev. B* **93** 075117
[14] Fang Y, Song Y Q, Zhou W P, Zhao R, Tang R J, Yang H, Lv L Y, Yang S G, Wang D H and Du Y W 2014 *Sci. Rep.* **4** 3860
[15] Kimura T, Goto T, Shintani H, Ishizaka K, Arima T and Tokura Y 2003 *Nature* **426** 55
[16] Wang J, Neaton J B, Zheng H, Nagarajan V, Ogale S B, Liu B, Viehland D, Vaithyanathan V, Schlom D G, Waghmare U V, Spaldin N A, Rabe K M, Wuttig M and Ramesh R 2003 *Science* **299** 1719
[17] Chapon L C, Blake G R, Gutmann M J, Park S, Hur N, Radaelli P G and Cheong S W 2004 *Phys. Rev. Lett* **93** 177402
[18] Seki S, Yu X Z, Ishiwata S and Tokura Y 2012 *Science* **336** 198
[19] Choi T, Horibe Y, Yi H T, Choi Y J, Wu W D and Cheong S W 2010 *Nat. Mater.* **9** 253
[20] Nagaosa N and Tokura Y 2013 *Nat. Nanotechnol.* **8** 899
[21] Romming N, Hanneken C, Menzel M, Bickel J E, Wolter B, von Bergmann K, Kubetzka A and Wiesendanger R 2013 *Science* **341** 636
[22] Huang F T and Cheong S W 2017 *Nat. Rev. Mater.* **2** 17004
[23] Du K, Gao B, Wang Y, Xu X, Kim J, Hu R, Huang F T and Cheong S W 2018 *npj Quantum Mater.* **3** 33
[24] Ponet L, Artyukhin S, Kain T, Wettstein J, Pimenov A, Shuvaev A, Wang X, Cheong S W, Mostovoy M and Pimenov A 2022 *Nature* **607** 81
[25] Wang H, Wang F, Yang M, Chang Y T, Shi M Y, Li L, Liu J M, Wang J F, Dong S and Lu C L 2025 *Phys. Rev. Lett.* **134** 016708
[26] Liu G, Pi M, Zhou L, Liu Z, Shen X, Ye X, Qin S, Mi X, Chen X, Zhao L, Zhou B, Guo J, Yu X, Chai Y, Weng H and Long Y 2022 *Nat. Commun.* **13** 2373
[27] Zhou Y, Ye H, Zhang J and Dong S 2024 *Phys. Rev. B* **110** 054424
[28] Liu Q, Cui S, Bian R, Pan E, Cao G, Li W and Liu F 2024 *ACS Nano* **18** 1778
[29] Gong C and Zhang X 2019 *Science* **363** eaav4450
[30] Zhang Y F, Guo H, Zhu Y, Song S, Zhang X, Luo W, Zhang Y Y and Du S 2024 *Adv. Funct. Mater.* **34** 2410240
[31] Song T, Fei Z, Yankowitz M, Lin Z, Jiang Q, Hwangbo K, Zhang Q, Sun B, Taniguchi T, Watanabe K, McGuire M A, Graf D, Cao T, Chu J H, Cobden D H, Dean C R, Xiao D and Xu X 2019 *Nat. Mater.* **18** 1298
[32] Yang L, Ding S, Gao J and Wu M 2023 *Phys. Rev. Lett.* **131** 096801
[33] Li L and Wu M 2017 *ACS Nano* **11** 6382
[34] Liu K, Ma X, Xu S, Li Y and Zhao M 2023 *npj Comput. Mater.* **9** 16
[35] Li L, Li X, Lin L, Zhang D, Chen M, Wu D and Yang Y 2024 *Phys. Rev. B* **110** 205119
[36] Zheng S H, Zhou G Z, Li X, Liu M F, Tang Y S, Xie Y L, Zeng M, Lin L, Yan Z B, Huang X K, Jiang X P and Liu J M 2020 *Appl. Phys. Lett.* **117** 072903
[37] Chang Y T, Wang J F, Wang W, Liu C B, You B, Liu M F, Zheng S H, Shi M Y, Lu C L and Liu J M 2023 *Phys. Rev. B* **107** 014412
[38] Maignan A and Martin C 2018 *Phys. Rev. B* **97** 161106
[39] Chang Y T, Weng Y K, Xie Y L, You B, Wang J F, Li L, Liu J M, Dong S and Lu C L 2023 *Phys. Rev. Lett* **131** 136701
[40] Kurumaji T, Ishiwata S and Tokura Y 2017 *Phys. Rev. B* **95** 045142
[41] Tang Y S, Wang S M, Lin L, Li C, Zheng S H, Li C F, Zhang J H, Yan Z B, Jiang X P and Liu J M 2019 *Phys. Rev. B* **100** 134112
[42] Tang Y S, Zhang J H, Lin L, Chen R, Wang J F, Zheng S H, Li C, Zhang Y Y, Zhou G Z, Huang L, Yan Z B, Lu X M, Wu D, Huang X K, Jiang X P and Liu J M 2021 *Phys. Rev. B* **103** 014112
[43] Zhang J H, Lin L, Tang Y S, Zhou G Z, Huang L, Li X Y, Li G Y, Zheng S H, Liu M F, Liu X M, Yan Z B, Huang X K, Chen C, Jiang X P and Liu J M 2023 *Phys. Rev. B* **108** 024107
[44] Shen X D, Zhou L, Chai Y S, Wu Y, Liu Z H, Yin Y Y, Cao H B, Cruz C D, Sun Y, Jin C Q, Muñoz A, Alonso J A and Long Y W 2019 *NPG Asia Mater.* **11** 50
[45] Tang Y S, Lin L, Zhou G Z, Zhai W J, Huang L, Zhang J H, Zheng S H, Liu M F, Yan Z B, Jiang X P, Li X A and Liu J M 2023 *Phys. Rev. B* **107** 214416
[46] Rivera J P 1994 *Ferroelectrics* **161** 147
[47] Vaknin D, Zarestky J L, Rivera J P and Schmid H 2004 *Phys. Rev. Lett* **92** 207201
[48] Li X, Liu M F, Wang Y, Tian L M, Shi R, Yang L, Pan Q Y, Han J J, Xie B, Zhao N, Wang X Z, Li S Z, Lin L, Yan Z B and Liu J M 2018 *Appl. Phys. Lett.* **113** 122903
[49] Lin L, Tang Y S, Huang L, Zhai W J, Zhou G Z, Zhang J H, Liu M F, Li G Y, Li X Y, Yan Z B and Liu J M 2022 *Appl. Phys. Lett.* **120** 052901

[50] Yu B, Wang S Y, Huang L, Tang Y S, Lin L, Zhou G Z, Zhang J H, Liu M F, Zheng S H, Yan Z B, Huang X K, Wang J F, Wan J G, Jiang X P and Liu J M 2024 *Phys. Rev. B* **109** 214435

[51] Yu B, Huang L, Li J S, Lin L, Ovidiu Garlea V, Zhang Q, Zou T, Zhang J C, Peng J, Tang Y S, Zhou G Z, Zhang J H, Zheng S H, Liu M F, Yan Z B, Zhou X H, Dong S, Wan J G and Liu J M 2024 *Phys. Rev. B* **109** 184106

[52] Zhang J H, Lin L, Zheng S H, Chen P Z, Huang L, Zhou G Z, Zhai W J, Yu F, Yu B, Cui X M, Liu M F, Tang Y S, Yan Z B and Liu J M 2024 *Appl. Phys. Lett.* **124** 172903

[53] Ma G Q, Zhou D, Xie Y L, Zheng S H, Liu M F, Tan L L, Liu Z, Liu F, Li Y, Ma Z, Zhang Y J, Lin L, Zeng M, Wang X Z, Wang S Y, Li H, Dong S and Liu J M 2025 *Journal of Materiomics* **11** 100977

[54] Xu X, Hao Y, Peng S, Zhang Q, Ni D, Yang C, Dai X, Cao H and Cava R J 2023 *Nat. Commun.* **14** 8034

[55] Astrov D N 1960 *J. Exptl. Theoret. Phys.* **38** 984

[56] Astrov D N 1961 *J. Exptl. Theoret. Phys.* **40** 1035

[57] Rado G T and Folen V J 1961 *Phys. Rev. Lett.* **7** 310

[58] Kosub T, Kopte M, Huhne R, Appel P, Shields B, Maletinsky P, Hubner R, Liedke M O, Fassbender J, Schmidt O G and Makarov D 2017 *Nat. Commun.* **8** 13985

[59] Du K, Xu X H, Won C, Wang K F, Crooker S A, Rangan S, Bartynski R and Cheong S W 2023 *npj Quantum Mater.* **8** 17

[60] Yuan W, Zhu Q, Su T, Yao Y Y, Xing W Y, Chen Y Y, Ma Y, Lin X, Shi J, Shindou R, Xie X C and Han W 2018 *Sci. Adv.* **4** eaat1098

[61] Makushko P, Kosub T, Pylypovskyi O V, *et al*. 2022 *Nat. Commun.* **13** 6745

[62] Zhang X S, Carbin T, Culver A B, Du K, Wang K F, Cheong S W, Roy R and Kogar A 2024 *Nat. Mater.* **23** 790

[63] Zheng S H, Liu M F, Zhou G Z, Li X, Lin L, Yan Z B and Liu J M 2021 *Ceram. Int.* **47** 14041

[64] Zhang J H, Tang Y S, Lin L, Li L Y, Zhou G Z, Yang B, Huang L, Li X Y, Li G Y, Zheng S H, Liu M F, Zeng M, Wu D, Yan Z B, Huang X K, Chen C, Jiang X P and Liu J M 2023 *Phys. Rev. B* **107** 024108

[65] Tokura Y, Seki S and Nagaosa N 2014 *Rep. Prog. Phys.* **77** 076501

[66] Wang Y, Pascut G L, Gao B, Tyson T A, Haule K, Kiryukhin V and Cheong S W 2015 *Sci. Rep.* **5** 12268

[67] Kurumaji T, Ishiwata S and Tokura Y 2015 *Phys. Rev. X* **5** 031034

[68] Wang W, Li P Z, Chang Y T, Liu M F, Lu C L, Lu X B, Zeng M and Liu J M 2021 *Appl. Phys. Lett.* **118** 112901

[69] Yang J K, Su D, He J C, Ji Y, Guo Q W, Meng Y, Li X F, Wang L Y, Shen X, Yao Y, Long Y W, Sun Y and Yu R C 2023 *Phys. Rev. B* **107** 104408

[70] Yang J K, Meng Y, Li X F, Wang L Y, Zhuang H Y, Zhang J, Shen X, Long Y W and Yu R C 2025 *Phys. Rev. B* **112** 024407

[71] Tang Y S, Zhou G Z, Lin L, Chen R, Wang J F, Lu C L, Huang L, Zhang J H, Yan Z B, Lu X M, Huang X K, Jiang X P and Liu J M 2022 *Phys. Rev. B* **105** 064108

[72] Chang Y T, You B, Xie Y L, Liu Y, Xiong R, Lu C L and Liu J M 2023 *Appl. Phys. Lett.* **123** 102402

[73] Oh Y S, Artyukhin S, Yang J J, Zapf V, Kim J W, Vanderbilt D and Cheong S W 2014 *Nat. Commun.* **5** 3201

[74] Zhang J H, Lin L, Dong C, Chang Y T, Wang J F, Lu C L, Chen P Z, Zhai W J, Zhou G Z, Huang L, Tang Y S, Zheng S H, Liu M F, Zhou X H, Yan Z B and Liu J M 2024 *Phys. Rev. B* **109** 184112

[75] Long Y W, Liu Q Q, Lv Y X, Yu R C and Jin C Q 2011 *Phys. Rev. B* **83** 024416

[76] Qi X L and Zhang S C 2011 *Rev. Mod. Phys.* **83** 1057

[77] Hasan M Z and Kane C L 2010 *Rev. Mod. Phys.* **82** 3045

[78] Lv B Q, Qian T and Ding H 2021 *Rev. Mod. Phys.* **93** 025002

[79] Mühlbauer S, Binz B, Jonietz F, Pfleiderer C, Rosch A, Neubauer A, Georgii R and Böni P 2009 *Science* **323** 915

[80] Yu X Z, Onose Y, Kanazawa N, Park J H, Han J H, Matsui Y, Nagaosa N and Tokura Y 2010 *Nature* **465** 901

[81] Yu X Z, Kanazawa N, Onose Y, Kimoto K, Zhang W Z, Ishiwata S, Matsui Y and Tokura Y 2010 *Nat. Mater.* **10** 106

[82] Sekiguchi F, Budzinauskas K, Padmanabhan P, Versteeg R B, Tsurkan V, Kézsmárki I, Foggetti F, Artyukhin S and van Loosdrecht P H M 2022 *Nat. Commun.* **13** 3212

[83] Yang K L, Zhang Y, Zheng S H, Lin L, Yan Z B, Liu J M and Cheong S W 2017 *Phys. Rev. B* **95** 024114

[84] Yang K L, Zhang Y, Zheng S H, Lin L, Yan Z B, Liu J M and Cheong S W 2017 *Phys. Rev. B* **96** 144103

[85] Ruff E, Widmann S, Lunkenheimer P, Tsurkan V, Bordács S, Kézsmárki I and Loidl A 2015 *Sci. Adv.* **1** e1500916

[86] Ruff E, Lunkenheimer P, Loidl A, Berger H and Krohns S 2015 *Sci. Rep.* **5** 15025

[87] Wang Z, Chai Y and Dong S 2023 *Phys. Rev. B* **108** L060407

[88] Alonso J A, Casais M T, Martínez-Lope M J, Martínez J L and Fernández-Díaz M T 1997 *J. Phys.: Condens. Matter* **9** 8515

[89] Yahia G, Damay F, Chattopadhyay S, Balédent V, Peng W, Kim S W, Greenblatt M, Lepetit M B and Foury-Leylekian P 2018 *Phys. Rev. B* **97** 085128

[90] Sheng J, Tong X, Ye F, Fernandez-Baca J A, Cao H, Poudel N, Gooch M, Lorenz B, Chu C W, Wang X and Cheong S W 2019 *Phys. Rev. B* **99** 094429

[91] Lee N, Vecchini C, Choi Y J, Chapon L C, Bombardi A, Radaelli P G and Cheong S W 2013 *Phys. Rev. Lett.* **110** 137203

[92] Bukhari S H, Kain T, Schiebl M, Shuvaev A, Pimenov A, Kuzmenko A M, Wang X, Cheong S W, Ahmad J and Pimenov A 2016 *Phys. Rev. B* **94** 174446

[93] Balédent V, Vaunat A, Petit S, Nataf L, Chattopadhyay S, Raymond S and Foury-Leylekian P 2023 *Phys. Rev. B* **108** 174446

[94] Shimakawa Y 2008 *Inorg. Chem.* **47** 8562

[95] Bizoń P, Maliborski M and Rostworowski A 2015 *Phys. Rev. Lett.* **115** 081103

[96] Long Y and Shimakawa Y 2010 *New J. Phys.* **12** 063029

[97] Long Y 2016 *Chin. Phys. B* **25** 078108

[98] Wang B, Zhang X, Zhang Y, Yuan S, Guo Y, Dong S and Wang J 2020 *Mater. Horiz.* **7** 1623

[99] Xiao D, Liu G B, Feng W, Xu X and Yao W 2012 *Phys. Rev. Lett.* **108** 196802

[100] Khanh N D, Abe N, Kimura S, Tokunaga Y and Arima T 2017 *Phys. Rev. B* **96** 094434

[101] Man P, Huang L, Zhao J and Ly T H 2023 *Chem. Rev.* **123** 10990

[102] Ren D H, Wen Y, Zeng H, Feng X Q, Zhang T, Zhang Y, Wang L S, Li Q, Du M, Zhou Z Y, Yi J Q and He J 2025 *Front. Phys.* **20** 044302

[103] Lui C H, Liu L, Mak K F, Flynn G W and Heinz T F 2009 *Nature* **462** 339

[104] Song Q, Occhialini C A, Ergeçen E, Ilyas B, Amoroso D, Barone P, Kapeghian J, Watanabe K, Taniguchi T, Botana A S, Picozzi S, Gedik N and Comin R 2022 *Nature* **602** 601

[105] Lai Y, Song Z, Wan Y, Xue M, Wang C, Ye Y, Dai L, Zhang Z, Yang W, Du H and Yang J 2019 *Nanoscale* **11** 5163

[106] Zhang J J, Lin L, Zhang Y, Wu M, Yakobson B I and Dong S 2018 *J. Am. Chem. Soc.* **140** 9768

[107] Kurumaji T, Seki S, Ishiwata S, Murakawa H, Kaneko Y and Tokura Y 2013 *Phys. Rev. B* **87** 014429

[108] Ju H, Lee Y, Kim K T, Choi I H, Roh C J, Son S, Park P, Kim J H, Jung T S, Kim J H, Kim K H, Park J G and Lee J S 2021 *Nano Lett.* **21** 5126

[109] Song Q, Stavrić S, Barone P, Droghetti A, Antonenko D S, Venderbos J W F, Occhialini C A, Ilyas B, Ergeçen E, Gedik N, Cheong S W, Fernandes R M, Picozzi S and Comin R 2025 *Nature* **642** 64

[110] Jiang Y, Wu Y, Zhang J, Wei J, Peng B and Qiu C W 2023 *Nature* **619** E40

[111] Amini M, Fumega A O, González-Herrero H, Vaňo V, Kezilebieke S, Lado J L and Liljeroth P 2024 *Adv. Mater.* **36** 2311342

[112] Wu Y, Zeng Z, Lu H, Han X, Yang C, Liu N, Zhao X, Qiao L, Ji W, Che R, Deng L, Yan P and Peng B 2024 *Nat. Commun.* **15** 8616

[113] Amoroso D, Barone P and Picozzi S 2020 *Nat. Commun.* **11** 5784

[114] Liu Q, Su W, Gu Y, Zhang X, Xia X, Wang L, Xiao K, Zhang N, Cui X, Huang M, Wei C, Zou X, Xi B, Mei J W and Dai J F 2025 *Nat. Commun.* **16** 4221

[115] Qi J, Wang H, Chen X and Qian X 2018 *Appl. Phys. Lett.* **113** 043102

[116] Wang X, Shang Z, Zhang C, *et al*. 2023 *Nat. Commun.* **14** 840

[117] Yang R, Zhang X, Xiao J, Yan Z, Wang F and Xu X 2025 *Chin. Phys. Lett.* **42** 070705

[118] Tu Z, Wu M and Zeng X C 2017 *J. Phys. Chem. Lett.* **8** 1973

[119] Huang C, Du Y, Wu H, Xiang H, Deng K and Kan E 2018 *Phys. Rev. Lett.* **120** 147601

[120] Zhao Y, Lin L, Zhou Q, Li Y, Yuan S, Chen Q, Dong S and Wang J 2018 *Nano Lett.* **18** 2943

[121] Yang H, Pan L, Xiao M, Fang J, Cui Y and Wei Z 2019 *Sci. China Mater.* **63** 421

[122] Zhao M, Chen J, Wang S S, An M and Dong S 2021 *Phys. Rev. Mater.* **5** 094408
[123] Wang C, You L, Cobden D and Wang J 2023 *Nat. Mater.* **22** 542
[124] Gong C, Kim E M, Wang Y, Lee G and Zhang X 2019 *Nat. Commun.* **10** 2657
[125] Sun W, Wang W, Li H, Zhang G, Chen D, Wang J and Cheng Z 2020 *Nat. Commun.* **11** 5930
[126] Yang W, Xu Y, Li S, Han J, Lin X and Zhao W 2025 *Sci. China Mater.* **68** 1622
[127] Yu X, Zhang X and Wang J 2023 *ACS Nano* **17** 25348
[128] Jiang X, Wang Z, Li C, Sun X, Yang L, Li D, Cui B and Liu D 2024 *Chin. Phys. Lett.* **41** 057501
[129] Li P, Tao L, Jin X, Wan G, Zhang J, Zhang Y F, Sun J T, Pan J and Du S 2024 *Nano Lett.* **24** 2345
[130] Xun W, Wu C, Sun H, Zhang W, Wu Y Z and Li P 2024 *Nano Lett.* **24** 3541
[131] Ye H and Dong S 2025 *Phys. Rev. Lett.* **135** 066701
[132] Shao Z, Liang J, Cui Q, Chshiev M, Fert A, Zhou T and Yang H 2022 *Phys. Rev. B* **105** 174404
[133] Papaioannou E T and Beigang R 2021 *Nanophotonics* **10** 1243
[134] Parchenko S, Hofhuis K, Larsson A Å, Kapaklis V, Scagnoli V, Heyderman L J and Kleibert A 2024 *Adv. Photonics Res.* **6** 2400083